UNIVERSITÀ
DEGLI STUDI
DI PADOVA

Sede Amministrativa: Università degli Studi di Padova

Centro Interdipartimentale di Studi e Attività Spaziali CISAS "G.Colombo"

SCUOLA DI DOTTORATO DI RICERCA IN: Scienze Tecnologie e Misure Spaziali
INDIRIZZO: Astronautica e Scienze da Satellite
CICLO: XXIV

A STUDY OF OPTICAL PULSARS FROM GAMMA TO RADIO FREQUENCY

Direttore della Scuola: Ch.mo Prof. Giampiero Naletto
Coordinatore d'indirizzo: Ch.mo Prof. Giampiero Naletto
Supervisore: Ch.mo Prof. Cesare Barbieri

Dottorando: Serena Gradari

Abstract

Questa tesi presenta uno studio delle pulsar ottiche in diverse bande di energia. L'approfondimento principale riguarda i risultati ottenuti nel visibile grazie all'uso di due fotometri, Aqueye e Iqueye, in grado di analizzare fenomeni astrofisici in rapida variazione. Una sezione della tesi è poi dedicata alla ricerca di nuove pulsar ottiche, selezionando possibili candidati a partire dai cataloghi di pulsar già note in altre lunghezze d'onda.

Le pulsar sono stelle di neutroni, ultimo stadio di evoluzione di alcune stelle massive, che ruotano rapidamente intorno al proprio asse. Presentano campi magnetici estremamente forti ed emettono fasci di particelle, che si muovono vicino o alla velocità della luce, in corrispondenza dei poli magnetici. La combinazione del meccanismo di rotazione e di emissione della radiazione è tale che, quando l'asse magnetico è diretto verso la Terra, siamo in grado di ricevere l'emissione pulsata della stella.

Il capitolo 2 della tesi illustra la teoria delle stelle di neutroni e delle pulsar. Dopo una breve introduzione storica, nella quale si racconta la scoperta della prima pulsar, PSR B1919+21 nel 1967, la fisica di queste stelle viene descritta, introducendo alcuni parametri. Tra questi, i più importanti, poiché verranno usati nel seguito della tesi durante l'analisi dei dati, sono il periodo

di rotazione e tutti i parametri che da esso derivano.

Considerando l'importanza che gli strumenti usati hanno avuto nell'ottenere i risultati esposti in questa tesi, nel terzo capitolo viene presentata una loro completa descrizione tecnica. Al momento, molti strumenti astronomici non sono in grado di distinguere i processi fisici che determinano l'emissione della radiazione da parte della sorgente. Per fare questo, è necessario misurare la statistica dei tempi di arrivo dei singoli fotoni, lavorando su tempi scala dell'ordine del picosecondo. Per esplorare dunque la possibilità di spingere gli strumenti astronomici oltre le loro attuali capacità in termini di risoluzione e *tagging* temporale, due fotometri ad alta velocità sono stati costruiti: Aqueye (Asiago Quantum Eye), per il telescopio da 1.8 m di Asiago (Italia), e Iqueye (Italian Quantum Eye), per il New Technology Telescope dell'ESO da 3.6 m che si trova a La Silla (Cile). Questi due strumenti sono fotometri ad apertura fissa in grado di raccogliere la luce entro un campo di vista di pochi arcosecondi intorno all'oggetto osservato.

Poiché è importante capire quali siano le prestazioni di questi strumenti quando si parla nello specifico di pulsar ottiche, uno studio originale è stato sviluppato proprio su questo tema, in particolare su Iqueye che è stato lo strumento principalmente usato nel corso di questa tesi. Lo scopo di questa analisi era quello di calcolare dal punto di vista teorico il numero di fotoni che ci si aspetta vengano registrati dai rivelatori, considerando la posizione dell'osservatorio e le caratteristiche delle tre principali pulsar ottiche (Crab, B0540-69 e Vela). Per ottenere questo risultato, è stato calcolato lo spettro del cielo a La Silla per poi combinarlo con lo spettro di efficienza complessiva di Iqueye. La stessa procedura è stata poi utilizzata usando gli spettri delle

tre stelle trovati nella letteratura. I risultati teorici sono stati poi comparati con i dati reali, in particolare con i risultati ottenuti dalle osservazioni della PSR B0540-69, la cui analisi è descritta in maniera approfondita nel capitolo 4. I risultati ottenuti hanno confermato la qualità dello strumento e la bontà delle nostre osservazioni, stabilendo inoltre un modo pratico per valutare la qualità delle future osservazioni.
In questo stesso capitolo viene descritto anche Aqueye, il primo prototipo costruito per il telescopio di Asiago. Per mostrare ciò che è possibile ottenere grazie a questo strumento, sono stati riportati i risultati delle osservazioni della pulsar Crab nel 2008. Da questi dati è stato possibile calcolare non solo la curva di luce ottica della pulsar, calcolando il periodo con una incertezza di 0.1 ns, ma anche fare un paragone tra la fase della Crab così ottenuta e quella riportata negli archivi radio presso il Jodrell Bank Observatory.

Il capitolo 4 descrive in maniera esaustiva le osservazioni della PSR B0540-69 nel 2009 che hanno portato alla pubblicazione di Gradari et al. (2011). La PSR B0540-69, che si trova nella Grande Nube di Magellano a una distanza d$\sim$ 49 kpc, è la seconda pulsar ottica più luminosa dopo la Crab. È stata osservata da Iqueye per diverse notti a gennaio e dicembre del 2009. Per poter effettuare un'analisi dettagliata del periodo e della curva di luce della stella, i tempi di arrivo dei fotoni sono stati anzitutto corretti rispetto al baricentro del sistema solare. Il periodo di rotazione della pulsar è stato quindi determinato usando una tecnica di *epoch-folding*. Già solo usando i nostri dati è stato possibile calcolare la derivata prima della frequenza. La curva di luce ottica derivata dalle nostre osservazioni è la prima acquisita dal 1996 e, considerando l'elevato numero di fotoni e l'accuratezza del *time-*

tagging garantita da Iqueye, ci sentiamo sicuri nell'affermare che si tratta anche della miglior curva di luce disponibile fino ad ora nel visibile.
Il calcolo della derivata prima e seconda della frequenza è stato poi effettuato aggiungendo i valori della frequenza trovati con Iqueye a quelli precedentemente pubblicati in letteratura. Con i valori così determinati del tempo, della frequenza e delle sue derivate prima e seconda, siamo stati in grado di calcolare il valore dell'indice di frenamento, $n = 2.080 \pm 0.015$, un parametro che permettere di fare alcune ipotesi sulla fisica della pulsar, e l'età caratteristica di questa stella, $\tau = 1677.5$ anni.

Infine, l'ultimo capitolo si concentra sull'analisi delle emissioni a diverse lunghezze d'onda. Poiché la ricerca di nuove pulsar ottiche è un compito complicato, l'idea è quella di cercare nei cataloghi di pulsar conosciute ad altre lunghezze d'onda per determinare quali possono essere possibili candidati ottici. Dopo una breve introduzione ai meccanismi di emissione nel radio e alle alte energie, la prima analisi riguarda l'emissione ottica delle pulsar radio. Usando dei modelli teorici precedentemente sviluppati, abbiamo isolato un gruppo di pulsar che sono risultate essere i candidati più interessanti. Un'analoga procedura è stata poi effettuata per le pulsar ad alta energia, in particolare usando i risultati nel gamma ottenuti dal telescopio Fermi. La parte originale sviluppata in questo ambito è consistita nell'intrecciare i risultati ottenuti ai due estremi dello spettro. Questo passaggio ha portato all'isolamento di una pulsar che sembra essere una possibile candidata sia nel radio che nel gamma: PSR B1706-44. Questa pulsar è già stata studiata in letteratura nell'ambito ottico ma finora non ci sono stati risultati a riguardo, probabilmente a causa dell'inadeguatezza degli strumenti. I risultati ottenuti

in questa tesi incoraggiano però ulteriori tentativi, possibilmente utilizzando telescopi più grandi, come il Very Large Telescope a Cerro Paranal (Chile) e strumenti ottimizzati per questo tipo di osservazioni, come potrebbe essere una nuova versione di Iqueye adattata per un telescopio più grande.

Abstract

This thesis reports a study of optical pulsars in different energy bands. The main focus is on the results obtained in the visible with two high speed photometers, Aqueye and Iqueye. A section is then dedicated to the search of new optical candidates, starting from the catalogs of known pulsars in other energy bands.

Pulsars are neutron stars, formed at the end of the evolution of massive stars, rapidly rotating around their axis. They have strong magnetic fields and jets of particles, moving near or at the speed of light, stream out of their magnetic poles. Thanks to this mechanism of rotation and beam radiation emission, when the magnetic axis is directed towards the Earth, we receive a pulse from the star.

The second chapter of this thesis illustrates the theory of neutron stars and pulsars. After a brief historical introduction, in which the story of the discovery of the first pulsar, PSR B1919+21 in 1967, is told, the physics of pulsars is described and some important parameters are introduced. Among them, the most important, since they will be used later in the analysis of real data, are those relative to the period of rotation of the pulsars and all the parameters derived from it.

Since the instruments used played an extremely important part in the achievement of the results of this thesis, in the third chapter there is a full technical description of them. At the moment, most astronomical instrumentation does not allow to directly distinguish the physical processes of the radiation source emission. To do that, it is necessary to measure the arrival time statistics of individual photons, considering timescales of the order of picoseconds. To explore the possibility of pushing the time resolution and time tagging capabilities of astronomical instruments beyond their current capabilities, two prototypes of high speed photometers were built: Aqueye (Asiago Quantum Eye), adapted for the Asiago (Italy) 1.8 m telescope, and Iqueye (Italian Quantum Eye), for the 3.6 m New Technology Telescope of ESO in La Silla (Chile). Both instruments are fixed-aperture photometers which collect the light within a field of view of few arcseconds around the target object.

Since it was important to understand the performance of these instruments when dealing with objects like optical pulsars, an original study was developed particularly on the capabilities of Iqueye, the main instrument used in this thesis. The aim was to calculate from a theoretical point of way the number of photons expected to be collected by the detectors of the instrument, considering the location of the observatory and the characteristics of the three main optical pulsars (Crab, B0540-69 and Vela). To do that, the spectrum of the sky in La Silla was derived and then combined with the global efficiency of Iqueye. The same was then done with the spectra of the three pulsars derived from the literature. The theoretical results were then compared with real data, particularly with those of PSR B0540-69, whose

observation and analysis are extensively described in chapter 4. The results confirmed the good quality of the instrument and of the observations, setting also a practical way to evaluate the quality of future observations.
In the same chapter there is also a description of Aqueye, the first prototype to be built for the smaller telescope of Asiago. To illustrate the important achievements of this instrument, the results obtained while observing the Crab pulsar in 2008 are illustrated. Using this instrument it was possible not only to derived the optical light curve of the pulsar, calculating a period with an uncertainty of 0.1 ns, but also to do a comparison between the phase of the Crab pulsar and that reported in the radio archive at the Jodrell Bank Observatory.

Chapter 4 fully describes the observations of PSR B0540-69 in 2009, whose analysis lead to the publication of an original paper: Gradari et al. (2011). PSR B0540-69, located in the Large Magellanic Cloud at a distance d$\sim$ 49 kpc, is the second brightest pulsar in the optical band after the Crab. It was observed by Iqueye for several nights in January and December 2009. In order to perform the detailed analysis of the period and light curve, the arrival times of the photons were first referred to the barycenter of the solar system. The spin period of the pulsar was then determined by an epoch-folding technique. Just with our data it was possible to determine the first derivative of the frequency. The optical light curve that was derived from our data is the first acquired since 1996 and, given the high number of photons and the extremely accurate time tagging guaranteed by Iqueye, we feel confident to say that it is also the best available so far in visible light.
We then calculated the first and second frequency derivatives of the pulsar

adding the frequency values measured by Iqueye to the previously published data sets. With the so determined values of time, frequency and frequency derivatives, we were able to calculate the braking index, $n = 2.080 \pm 0.015$, a parameter that provides insight into the physics of the pulsar mechanisms, and the characteristic age of the pulsar, $\tau = 1677.5$ years.

Last chapter was dedicated to the multiwavelength emission analysis. Since searching for a new optical pulsar is a difficult task, the idea was to look through the catalogs of known pulsars in other wavelengths to determine which ones can be possible optical candidates. After a brief introduction of the emission mechanisms in radio and in high energy bands, the optical emission of radio pulsars was first introduced. Using models already developed in the past, a group of pulsars was isolated, being the most interesting candidates. The same procedure was then applied to high energy pulsars, using the results obtained in gamma by the Fermi telescope. The original part developed in this thesis was done by correlating the results found at the two extreme of the spectrum. This led to the isolation of a pulsar that appears to be a possible optical candidates both in radio and in gamma: PSR B1706-44. It was found in the literature that this pulsars was already considered an interesting candidate. However, until now, optical observations led to nothing, probably due to the inadequacy of the instruments. The results found in this thesis encourage further surveys, possibly using bigger telescope, like the Very Large Telescope in Cerro Paranal (Chile), and optimized instruments, like a newer version of Iqueye adapted for a bigger telescope.

Alla mia famiglia.

Contents

Chapter 1

Introduction

Pulsars are neutron stars in rapid rotation around their own axis. These objects can be formed at the end of the evolution of massive stars, when the star's core collapses to a neutron star and the star's shell is ejected (supernova explosion). They have a very strong magnetic field and jets of particles moving near or at the speed of light stream out of their magnetic poles. In this way, when the magnetic axis is directed towards the Earth, we receive a pulse from the star.

Despite more than forty years of observations, there are still several unanswered question in pulsar astrophysics. In the optical band questions are even more profound: first of all, why there is only a small number of observed optical pulsars with respect to the larger number in the other spectral bands? So far, optical pulsation has been detected only from 5 pulsars: PSR B0531+21 (Crab pulsar), PSR B0540-69, PSR J0633+1746 (Geminga pulsar), PSR B0656+14, PSR B0833-45 (Vela pulsar). This could be due to the fact that only a few percentage of pulsars emit in the optical or, more

probably, to the lack of adequate instruments for the observations.

To explore the possibility of pushing the time resolution and the time tagging capabilities of astronomical instruments beyond their current capabilities, two prototypes of high speed photometers were built in order to acquire experience: Aqueye (Asiago Quantum Eye) and Iqueye (Italian Quantum Eye). Both instruments were used to observe optical pulsars.

Aqueye, built for the Asiago (Italy) 1.8 m telescope, was the first photometer to be built. Since the beginning, it gave great results, particularly on the Crab pulsar, and was a necessary step to take in order to built the second prototype, Iqueye, designed for a bigger telescope. Iqueye, the main instrument used for the study of optical pulsars during this thesis, is a fast photon counting photometer built specifically to be mounted on the 3.5 m New Technology Telescope (NTT) at La Silla Observatory (Chile). These instruments were the first attempts to overcome the difficulties in the observation of optical pulsars by using instruments capable of properly analyze the timing signature of rapidly varying sources.

Part of the work reported in this thesis was done with Iqueye, both from a theoretical and an experimental way. The former aspect was approached from the point of view of the performance of the instrument when dealing with astrophysical objects like optical pulsars. The procedure conceived and adopted is described in section 3.2. The idea was to calculate the theoretical number of photons expected when observing the three main optical pulsars (Crab, B0540-69 and Vela) and then compare the results with real data. In doing that, it was also necessary to calculate the spectrum of the sky in La Silla and combine it with the efficiency spectrum of Iqueye. The procedure

adopted demonstrated the good quality of our data and also resulted to be a practical way to test the quality of future observations.

From an experimental point of view, Iqueye was tested during the nights of observation carried out in 2009. Chapter 4 fully describes the observations of PSR B0540-69. The analysis of the collected data led to the publication of an original paper: Gradari et al. (2011). The most important result of this work was the publication of the optical light curve of this pulsar: it was the first published since 1996. Given the high number of photons and the extremely accurate time tagging guaranteed by Iqueye, we feel also confident to say that this light curve (Figure 4.2) is also the best available so far in visible light. With our data alone, obtained over a time span of one year, we were able to determine the first derivative of the frequency, a value in good agreement with those available in the literature. Adding our values to previously published data sets, it was then possible to determine also the second frequency derivative. With the so determined values of time, frequency and frequency derivatives, we were able to calculate the braking index, a parameter that provides insight into the physics of the pulsar mechanism, and the characteristic age of the pulsar.

A third important analysis that has been done in this thesis is described in Chapter 5. A multiwavelength emission analysis was carried out in order to find new possible pulsar condidates for future optical observations. Starting from pulsar emission models found in the literature, some possible candidates were found both in radio and in gamma. The correlation between the results found at the two extreme of the spectrum led to the isolation of a pulsar as the most interesting candidate: PSR B1706-44 (Section 5.3). Even if, until now,

optical observations of this pulsar led to no results, the theoretical outcomes of this thesis encourage further surveys, possibly with bigger telescopes and optimized instruments.

Chapter 2

Theory of pulsars

2.1 History

In 1932, Walter Baade (Mt. Wilson Observatory) and Fritz Zwicky (Caltech) proposed for the first time the idea of the existence of stars composed almost entirely by neutrons, called neutron stars, born in the core of supernovae. A few years later, in 1939, Oppenheimer and Volkoff presented the first model of the structure of such a star (Oppenheimer & Volkoff 1939).

The first serious attempts to discover neutron stars were made in the 1960s, trying to detect the thermal radiation in the X-ray band from the surface of cooling isolated neutron stars. In the meantime, radio astronomy innovations leaded to the unexpected discovery of quasars. Following this discovery, Antony Hewish and his student Jocelyn Bell of the University of Cambridge decided to try to differentiate the quasars of radio-galaxies using interplanetary scintillation, refraction of radio waves due to terrestrial atmosphere and interstellar ionised gas. To this aim, they built a new ra-

diotelescope: it was an array of 2048 dipole antennae that covered an area of about 18.000 square meters and it's wavelength was 3.7 m. The telescope differed from the other ones for its really good temporal resolution. On August 6, 1967 Bell discovered a weak variable radio source at 19h19m of Right Ascension and +21° of Declination (Figure 2.1). By the end of September, the source had been observed several times: at the beginning it was suggested to be a flare star. By November 28, the observations had indicated that the source had emitted strictly periodic pulses. The accurate measurement of the period started in December 11. The period turned out to be extremely stable: 1.3373012 s. This produced a suspicious that the signals were of artificial origin. It took several weeks to understand that the rapidly pulsating source, called pulsar, was well outside the Solar System. This object is now known as PSR B1919+21 [1] (Hewish et al. 1968).
By the beginning of February, 1968, three other pulsars had already been discovered (PSR B1133+16, PSR B0834+06, and PSR B0950+08).

The link between pulsars and neutron stars was already been made before the discovery of PSR B1919+21. Pacini, studying the Crab nebula, postulated that its source of energy was a neutron star highly magnetised and rapidly spinning (Pacini 1967): a rapidly rotating neutron star with a strong dipole magnetic field could efficiently transform its rotational energy into electromagnetics radiation and, subsequently, accelerate particles to high energies. He suggested that the rotational energy loss rate is the same

[1] The pulsars discovered from 1967 until the mid 90 derive their name by their position in the sky following the system of equatorial besselian coordinates (B1950) preceded by a B: PSR Bxxxx+yy. Those discovered subsequently are named according to their position in the Julian system (J2000) preceded by a J: PSR Jxxxx+yyyy.

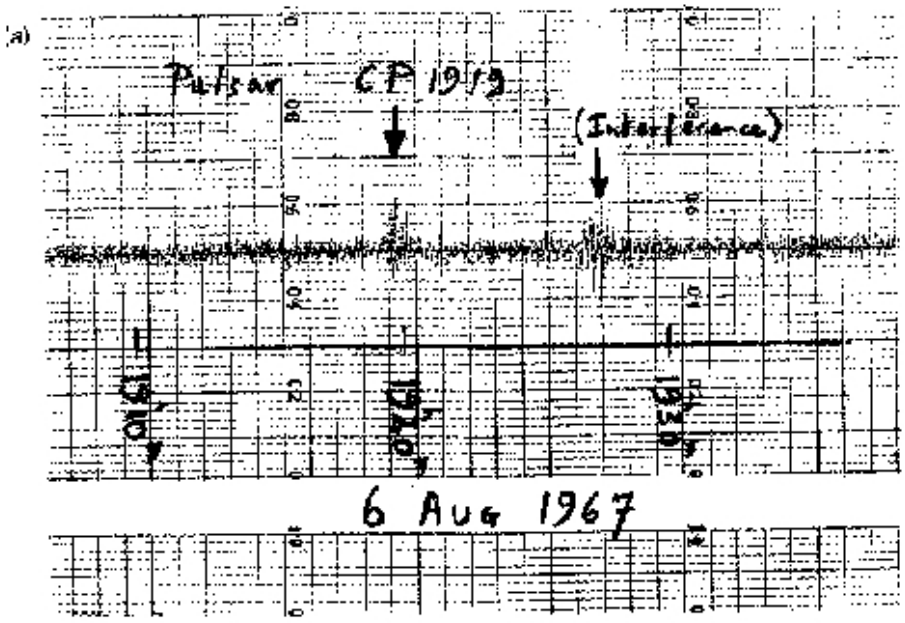

Figure 2.1: Discovery observations of the first pulsar. The first recording of PSR B1919+21; the signal resembled to radio interference also seen on the same plot.

as produced by a magnetic dipole rotating in vacuum. At the same time, Gold introduced the idea that pulsars are rotating magnetized neutron stars (Gold 1968). Rotating neutron stars can be considered similar to rotating magnetic dipole: they lose energy by elettromagnetic radiation and with the emission of relativistic particles. The decrease in energy leads to a gradual decrease in the period of rotation.

The discovery of a pulsar with period 89 ms in the core of the Vela supernova (Large et al. 1968) and of a pulsar with period 33 ms in the core of the Crab Nebula (Staelin & Reifenstein 1968) established the identity of pulsars as a neutron stars permanently.

2.2 Neutron stars

Neutron stars are the final products of stellar evolution. It is widely accepted that they are born in supernova explosions after their progenitors (giant or supergiant stars) exhaust nuclear fuel in their cores. The cores undergo gravitational collapse and become neutron stars (or black holes), while the outer layers are blown away by an expanding shock wave, producing supernova remnants. The whole event is usually referred to as core-collapse (type II) supernova explosion. Neutron stars can also be formed via a collapse of accreting white dwarfs in binary systems, after the white dwarf mass exceeds the Chandrasekhar limit. But the number of neutron stars formed in this way is expected to be small.

Neutron stars have typical masses $M \sim 1.4$ $M_\odot$ and radii $R \sim 10$ km. Thus, their masses are close to the solar mass $M_\odot = 1.989 \times 10^{33}$ g, but their

radii are $\sim 10^5$ times smaller than the solar radius $R_\odot = 6.96 \times 10^5$ km. Accordingly, neutron stars possess an enormous gravitational energy E_{grav} and surface gravity g:

$$E_{grav} \sim GM^2/R \sim 5 \times 10^{53}\text{erg} \sim 0.2Mc^2, \tag{2.1}$$

$$g \sim GM/R^2 \sim 2 \times 10^{14}\text{cm s}^{-2}, \tag{2.2}$$

where G is the gravitational constant and c is the speed of light. Clearly, neutron stars are very dense. Their mean mass density is:

$$\bar{\rho} \sim 3M/(4\pi R^3) \sim 7 \times 10^{14}\text{g cm}^{-3} \sim (2-3)\rho_0, \tag{2.3}$$

where $\rho_0 = 2.8 \times 10^{14}$ g cm^{-3} is the so called normal nuclear density, the mass density of nucleon matter in heavy atomic nuclei. The central density of neutron stars is even larger, reaching (10-20)ρ_0: neutron stars are the most compact stars known in the Universe.

According to modern theory (see Page & Reddy (2006)), a neutron star consists of a very thin atmosphere, an envelope, a crust, and an outer core. The envelope is the thinnest, i.e. a few tens of meters, and the crust has a thickness of about 500 - 1000 meters (see Figure 2.2).

Between the surface of the star and its core, the volume density varies from 10^6 to 10^{15} g cm^{-3}. The star is composed of a rigid surface crust of a thickness of 1 km formed essentially of iron nuclei and a nucleus of neutron superfluid. The separation between these two parties is close to $\rho = 4.3 \times 10^{11}$ g cm^{-3}. Most models of dense matter predict a deconfinement of quarks and

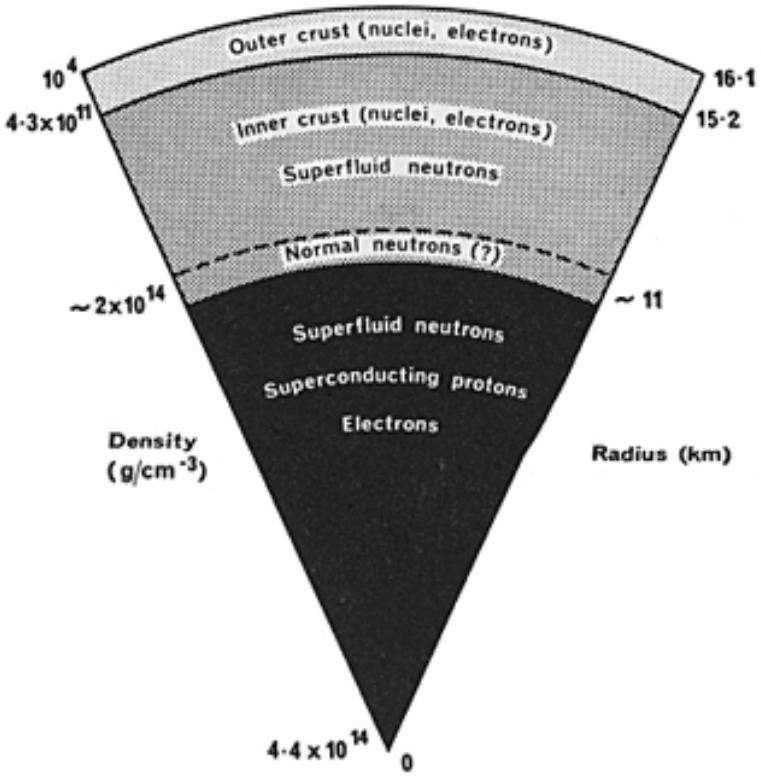

Figure 2.2: A slice of a neutron star showing the internal structure (Credit: NASA).

a possible appearance of exotic matter over a density of $\sim 5 \times 10^{14}$ g cm^{-3}, the density of cold nuclear matter. This structure, made up of different states of matter, could explain both the observation of perturbations of the rotation of the pulsar, called timing noise, and the sudden acceleration of the rotation period of pulsars, which are called glitches (Anderson & Itoh 1975; Janssen & Stappers 2007). Glitches give an unique opportunity to study the internal structure of neutron stars, as they are believed to be caused by sudden and irregular transfer of angular momentum from the superfluid inner parts of the star to the more slowly rotating crust. Glitches are observed as sudden jumps, $\Delta\Omega$, of the pulsar spin frequency $\Omega = 2\pi/P$ followed by a slow partial relaxation to a pre-glitch regular spindown ($\dot{P} > 0$). Relaxation time scales range over the period of days, months or years. The relative frequency jumps $\Delta\Omega/\Omega$ vary from $\sim 10^{-10}$ to $\sim 5 \times 10^{-6}$. Glitches are mainly observed from relatively young pulsars.

The equation of state of dense matter in neutron star interiors defines the radial density profile of the star and therefore the moment of inertia $I = kMR^2$. For a sphere of homogeneous density, we have $k = \frac{2}{5}$, while the models predict values ranging between 0.3 and 0.45 when the ratio M/R is between 0.1 and 0.2 $M_\odot$ (Lattimer & Prakash 2001). Using $k = 0.4$, $M = 1.4$ $M_\odot$ and $R = 10$ km, we obtain $I = 10^{45}$ g cm^2. This value is very uncertain: it could vary greatly from one pulsar to another, especially if there is accretion of matter during the lifetime of the neutron star.

2.3 Pulsars

Pulsars are spinning neutron stars with their magnetic moments inclined to spin axes. Their radio emission is generated outside the star, in the magnetosphere, and it is beamed along the magnetic axis. The beamed radiation rotates with the star so that a pulsar is detected if its beam crosses the Earth. The emitted electromagnetic radiation carries away the rotational energy and momentum and produces a slow regular spin-down of the pulsar (an increase of the pulse period).

Several essential properties of pulsars can be understood by assimilating them to rotating magnetic dipoles. The magnetic dipole field, whose axis is not necessarily aligned with the axis of rotation, induces an electric field $\vec{E} \propto (\vec{\Omega} \times \vec{r}) \times \vec{B}$, where $\vec{\Omega}$ is the angular velocity and $\vec{B}$ is the magnetic field prevailing at the distance $\vec{r}$. At equilibrium, the magnetosphere is filled with a charge distribution $\rho = -\vec{\Omega} \cdot \vec{B}/(2\pi c)$ and the $E_{||}$ component of the electric field is screened. The charged particles and the electric and magnetic fields of the magnetosphere start to co-rotate with the star.

A pulsar with a rotation period P is surrounded by an imaginary cylinder of light with a radius $cP/(2\pi)$, that is in co-rotation with the pulsar: so the surface moves at the speed of light (see Figure 2.3). Field lines which cross the light cylinder do not return to the surface of the neutron star and are referred to as open field lines. Otherwise, they are referred as closed field lines. It is believed that the space of closed field lines is filled by the Goldreich-Julian plasma distributed in such a way that the electric field created by charged particles in the pulsar-corotating reference frame compensates the projection

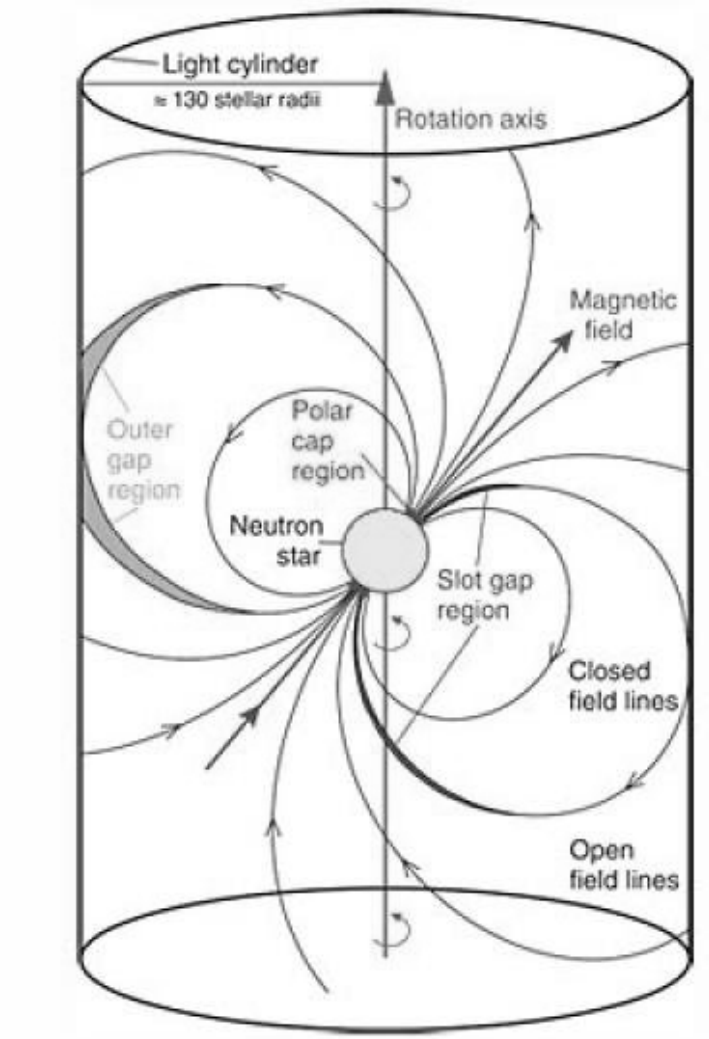

Figure 2.3: The lighthouse model of a pulsar: the pulsar is surrounded by a plasma-filled superconducting magnetosphere that rotates rigidly with the star except where there are open field lines. The light cylinder marks the boundary where plasma rotates at the speed of light to stay with the pulsar. Particles accelerated across vacuum gaps in the magnetosphere emit the electromagnetic radiation. (Credit: Magic Collaboration)

of the electric field, induced by the pulsar magnetic field, onto magnetic field lines. The space of closed magnetic field lines is inactive for particle acceleration and radiation generation. Therefore, the main magnetospheric activity is limited by the region of open magnetic field lines in the corotation zone. The edge of the polar cap is defined by the locus of the last closed magnetic field lines (i.e. the field lines which just touch the light cylinder). Open field lines let escape the charged particles above the magnetic poles. Charged particles generate the emission of photons whose directions are defined by the last open field lines, those that intercept the light cylinder. So, an emission beam centered around the magnetic axis of the pulsar is formed: if the beam intercepts the path of the Earth, a terrestrial observer can detect a periodic signal, repeated at each rotation of the pulsar (Lorimer & Kramer 2005). In different places of the magnetosphere the charged particles emit radiation in different spectral bands, with different beaming and polarization. As a result, a powerful (non-thermal) magnetospheric emission is created in the widest spectral range, from radio waves to hard γ-rays, accompanied by a flow of highly energetic particles. The latter flow produces a pulsar wind which feeds up pulsar wind nebulae.

2.3.1 Emission model

The pulsar emission can be separated into core emission and cone emission, both having the same axis. Since the neutron star rotates, the radiation emitted sweeps the sky and, as it passes the Earth, the pulsed emission can be observed.

If the line of sight is at the edge of the cone, the pulsar shows a single peak. If instead the line of sight cuts through the beam, closer to the core, then the pulse profile is double. Closer to the core, one observes a triple profile (Figure 2.4). The form of the pulse profile depends on the angle between the rotation axis and the axis of the dipole magnetic field. It also depends on the opening angle of the cone and on the angle between the rotation axis and the line of sight.

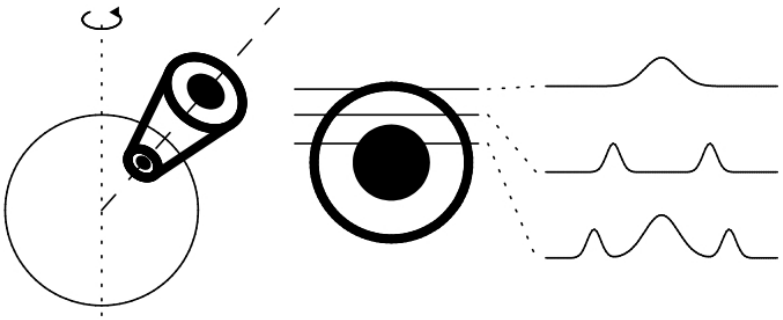

Figure 2.4: Sketch of the radiation beam, with core and cone, of a radio pulsar, and of the observed profile in different directions. (Credit: Frank Verbunt and John Heise, Astronomical Institute Utrecht)

Statistically, it appears that the opening angle of the cone is smaller for pulsars with long periods. We roughly have:

$$\rho = 6.4^\circ (\frac{P}{1\mathrm{s}})^{-1/3} \tag{2.4}$$

where ρ is the opening angle and P the pulse period. For slowly rotating pulsars, the beaming factor f is about 0.2, while faster rotating pulsars have larger cones and are more easily detected.

Depending on the magnetic field strength and its geometry, on relative orientation of magnetic and spin axes, and on the magnetospheric processes, it is possible to obtain different models of active magnetospheric zones. Some models, called polar cap models, place these zones in the vicinity of magnetic poles, near the pulsar surface. Other models, called outer gap models, locate the active magnetospheric zones much higher, above the surface, in the outer magnetosphere.

The total pulsar spin-down loss rate $\dot{E}_{spin}$ is thought to be approximately the same as produced by a magnetic dipole radiation in vacuum, but the entire physics is different. In particular, only a small fraction ($\sim 10^{-6}$) of $\dot{E}_{spin}$ is radiated away at radio frequencies while the rest is emitted in high-energy bands and in the form of pulsar wind, which may create a pulsar wind nebula (Haensel et al. 2007).

A magnetic dipole rotating in vacuum will induce an electric field both along and across the magnetic field lines. In a pulsar with high angular velocity Ω and surface dipole fields $B_0 \sim 10^{12}$ G, the electric force parallel to the magnetic field exceeds the gravitational force by many orders of magnitude. This implies that charges can be pulled from the stellar surface so that vacuum conditions cannot exist outside the pulsar (Goldreich & Julian 1969).

If the charge density reaches the Goldreich-Julian value,

$$\rho_{GJ} = \frac{\nabla \cdot \mathbf{E}}{4\pi} \sim -\frac{\mathbf{\Omega} \cdot \mathbf{B}}{2\pi c},$$

derived from the condition

$$\mathbf{E} = -\frac{(\Omega \times r) \times B}{c},$$

then the electric field parallel to the magnetic field vanishes. In this case, called the force-free solution, charges and magnetic field co-rotate with the star. This situation breaks down near the light cylinder. Since no acceleration of charges would exist in a completely force-free magnetosphere, a real pulsar must operate somewhere between the two extremes of the vacuum and the force-free states. Unfortunately, an exhaustive solution has not yet been found (Harding 2007).

2.4 Period and derived quantities

There are at least two sources of energy loss for the pulsar and its magnetosphere: the emission of dipole radiation at low frequencies, due to the rotation of the magnetic moment, and the escape of charged particles along the open field lines, resulting in a beam of emission along the magnetic axis. The rotational kinetic energy $E = \frac{1}{2} I \Omega^2$, where I is the moment of inertia of the neutron star and $\Omega = 2\pi/P$ is the angular velocity, is the main reservoir of energy of the pulsar. The decrease of E with a rate $\dot{E} = -I\Omega\dot{\Omega}$ leads to a slowing down of the rotation of the pulsar, with a rate $\dot{P} = -2\pi\dot{\Omega}/\Omega^2 > 0$. The quantity $\dot{E}$ is the energy loss due to the braking (spin-down power).

Depending on the parameters P and $\dot{P}$ and taking $I = 10^{45}$ g cm^2, we have:

$$\dot{E} = 4\pi^2 I \frac{\dot{P}}{P^3} \sim 3.95 \times 10^{31} \text{erg/s} \, (\frac{P}{1\text{s}})(\frac{\dot{P}}{10^{-15}})^{-3} \tag{2.5}$$

Since the moment of inertia I is almost independent of the detailed model adopted for the structure of the neutron star, and not much dependent on its mass, this total energy output is calculable for any pulsar directly from the measured values of P and $\dot{P}$.

These pulsars whose period increases with time due to their loss of rotational energy form the category of Rotation-Powered Pulsars. Another category of objects is the Accretion-Powered Pulsars. In this case, the radiation is due to the fall of matter from a companion star. The high temperature acquired by matter in its fall creates hot spots on the surface of the neutron star. These areas emits X-rays and rotates with the pulsar, creating a pulse signal.

Assuming that the loss of rotational kinetic energy of the pulsar is due to the magnetic dipole radiation exclusively, we have:

$$\dot{E} = -I\Omega\dot{\Omega} = \frac{2}{3c^3}\vec{\mu}^2\Omega^4 \sin^2(\alpha) \tag{2.6}$$

In this equation, $\vec{\mu}$ is the magnetic dipole momentum of the pulsar and α is the angle between the magnetic and the rotation axis. It results:

$$\dot{\Omega} = -(\frac{2\vec{\mu}^2 \sin^2(\alpha)}{3Ic^3})\Omega^3 \tag{2.7}$$

This last equation is the special case of $\dot{\Omega} \propto \Omega^n$ for a purely dipolar

energy loss, $n = 3$. The quantity n is called braking index. This index can be measured. In fact, $\dot{\Omega} \propto \Omega^n$ implies

$$n = \frac{\Omega\ddot{\Omega}}{\dot{\Omega}^2} \tag{2.8}$$

and Ω, $\dot{\Omega}$ and $\ddot{\Omega}$ can be obtained via the chronometry of pulsars. In practice, measurements of n are rare since $\ddot{\Omega}$ is often contaminated by instabilites of the rotation (timing noise). It is generally admitted that the gap between the braking index measurements and the theoretical value of 3 is the proof that an important part of the kinetic energy is dissipated via a wind of charged particles and of magnetic field emitted by the pulsars. The measurement of the braking index is hampered by the occurrence of discontinuous changes, glitches, in the period and the period derivative. In addition to the period derivative, the second derivative and the glitches, well observed pulsars like the Crab shows irregular wanderings in the pulse period.

The relationship of proportionality $\dot{\Omega} \propto \Omega^n$ can be integrated, provided that $n \neq 1$, to estimate the age of the pulsar:

$$T = \frac{P}{(n-1)\dot{P}}[1 - (\frac{P_0}{P})^{n-1}] \tag{2.9}$$

In this equation, T denotes the age of the pulsar, P and $\dot{P}$ are the current values of the period and its first derivative, and P_0 is the period of the pulsar at birth. Assuming that the initial period P_0 is negligible compared to the current period and that the origin of the slowdown is dipolar (or $n = 3$), we

have:

$$T = \tau = \frac{P}{2\dot{P}} \tag{2.10}$$

The quantity τ is called characteristic age.

Finally, the values of P and $\dot{P}$ and the dipole model can estimate the magnetic field prevailing in different parts on the magnetosphere, particularly on the surface of the pulsar and on the light cylinder. The magnetic field induced by the dipole moment at a distance r is given by:

$$B(r) = \frac{1}{r^3}\sqrt{-\frac{3Ic^3}{2\sin^2\alpha}\frac{\dot{\Omega}}{\Omega^3}} = \frac{1}{r^3}\sqrt{\frac{3Ic^3}{8\pi^2\sin^2\alpha}P\dot{P}} \tag{2.11}$$

Let B_S be the magnetic field at the surface and B_{LC} the magnetic field at the light cylinder, of radius $R_L = cP/(2\pi)$. For a canonical pulsar with a radius $R = 10$ km, moment of inertia $I = 10^{45}$ g cm^2, and choosing a magnetic inclination angle α equal to 90°, we have:

$$B_S = B(R) \sim 3.2 \times 10^{19}\text{G}\,\sqrt{P\dot{P}}B_{LC} = B_S(\frac{2\pi R}{cP})^3 \tag{2.12}$$

Note that such equations use a dipolar description of the field, while measures of the braking index indicate a more complex mechanism of rotational energy loss.

2.5 Different types of pulsar

We saw that pulsars lose energy over time, which results in a decrease in their rotation period. A very useful figure in order to study the evolution of

pulsars is the $P - \dot{P}$ diagram (Figure 2.5).

As the figure shows, the majority of known pulsars have a rotation period P between 0.1 and a few seconds, and a $\dot{P}$ between 10^{-17} et 10^{-13}. These are called normal or ordinary pulsars. It is estimated that they are born with a period between 14 and 140 ms (Kramer et al. 2003). The majority of normal pulsars is relatively young: a few thousand to tens of millions of years typically. It is possible to observe in the diagram an area depopulated of pulsars, in the bottom right corner of the graph, called graveyard. The small number of pulsars detected in this range of (P, $\dot{P}$) suggests that there must be a limit from which the pulsars stop to emit radiation detectable at great distances. In the diagram, radio pulsars evolve towards the right, as their period increases. The majority of radio pulsars have $B \sim 10^{12}$ G, although a few of them have much higher B. Old and slowly rotating isolated neutron stars induce much weaker electric fields (in their comoving reference frames) and cannot produce powerful outflow of charged particles from their surfaces. In this way they cannot support their magnetospheric activity and cease to operate as radio pulsars. These neutron stars (dead pulsars) have large P and small $\dot{P}$ and can be placed in the corresponding corner of the $P-\dot{P}$ diagram, separated from the main part of the diagram by the so called pulsar death line (*Graveyard* in Figure 2.5).

Finally, we find in the lower left of the graph the millisecond pulsars (MSPs), which stand out from the majority of ordinary pulsars by an extremely fast ($P < 30$ ms) and stable ($\dot{P} < 10^{-17}$) rotation.

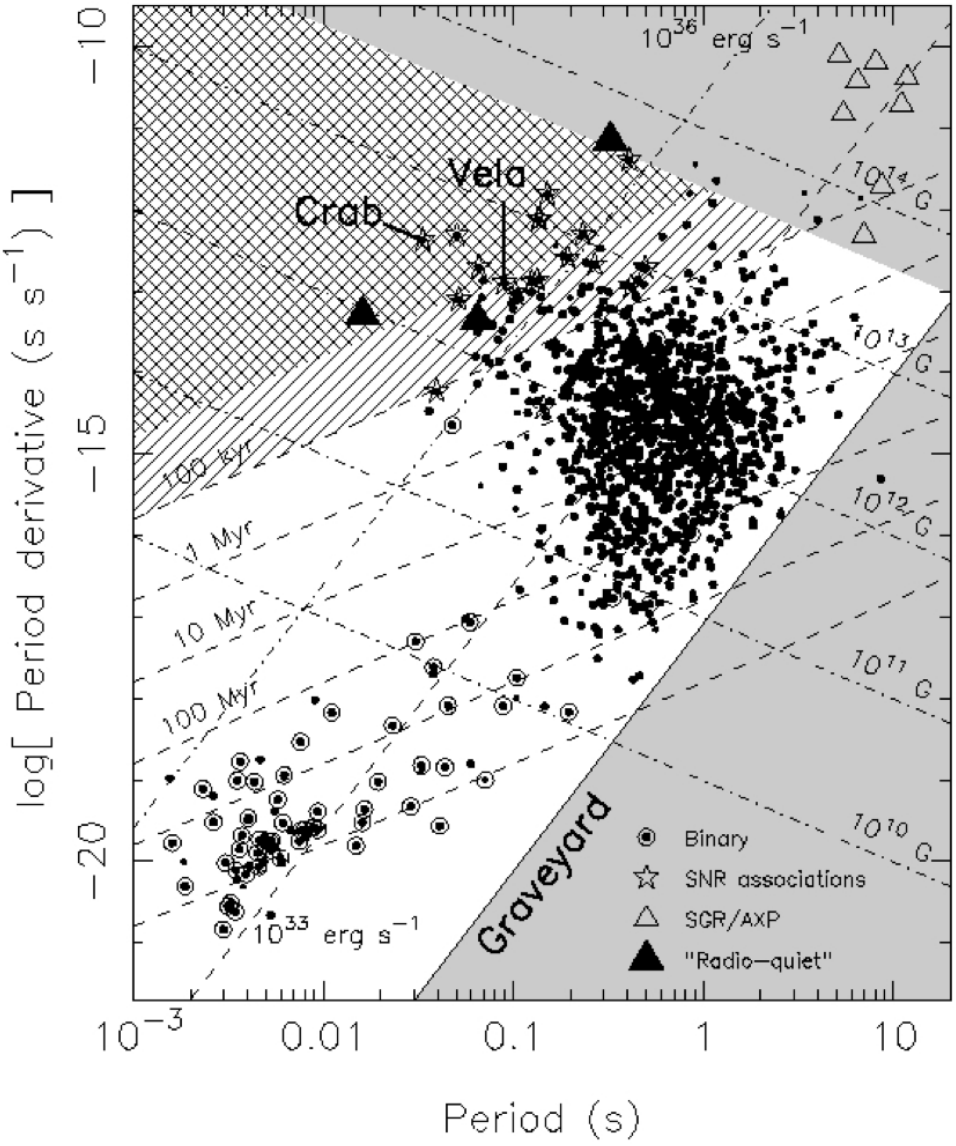

Figure 2.5: This diagram is useful for following the pulsars. It encodes informations about the pulsar population and its properties, as determined and estimated from its two of the primary observables. Using those parameters, one can estimate the pulsar age, magnetic field strength B, and spin-down power (Credit: Lorimer & Kramer (2005)).

2.5.1 Pulsar distribution

The majority of known pulsars come from the observations of the radiotelescopes of Jodrell Bank (England, Hobbs et al. 2004), Green Bank Telescope (USA, Kaplan et al. 2005), Nancay (France, Theureau et al. 2005), Arecibo (Porto Rico, Dowd et al. 2000), and Parkes (Australia, Manchester 2008). If we take a look at the distribution in galactic coordinates of the discovered pulsars in our Galaxy and in the Magellanic Cloud, we can see that this distribution is limited by the sensibility of the instruments and there's a bias in the choice of the observed region. Besides, the observed pulsars are strongly selected on the base of their apparent flux, $F \propto L/d^2$: pulsars with a low luminosity, L, can be seen only at short distances, d. Also, the effects of the interstellar medium on the radio signal propagation are really important on the galactic plane, particularly approaching the centre. The consequence of all these effects is that the current sample represents just a small portion of the population of active pulsars in the Galaxy, estimated between 10^5 and 10^6 (Lyne et Graham-Smith, 1998).

There are several methods to evaluate the distance of pulsars, either the measure of their parallax, or by measuring the dispersion of the radio signal with a model of the distribution of density or by the absorption of neutral hydrogen and the association of object. The spectra of pulsars situated at low galactic latitude, inside the arms of the Galaxy, can show an absorption line of the neutral hydrogen. The hydrogen, in the form of cloud, absorbs at the wavelength of 21 cm (1420 MHz). This HI line can show a spectral gap, due to the Doppler effect, caused by the movement of gas inside the spiral

arms.

Pulsars are distributed on the galactic plane as massive O and B stars, with a thickness of about 1 kpc on a radius of 10 kpc around the galactic centre (Figure 2.6). This observation reinforces the hypothesis that neutron stars are born from the gravitational collapse of massive stars. It also appears that many pulsars are outside the plan: it is possible that violent explosions of supernova are not completely symmetrical, giving the pulsar an impulse at the pulsar birth (Janka et al. 2005). The measurement of proper motions of a sample of 233 pulsars shows an average speed of propagation of 246 ± 22 km/s (Hobbs et al. 2006). The fastest can reach 1000 km/s. The consequence is that a significant fraction of pulsars escape from their supernova remnant, and, subsequently, the galactic plane.

The properties of pulsars in binaries are different from those of single pulsars because they have accreted matter from the companion star in the past. Many such pulsars have been spun up to very short rotation periods and are often called millisecond pulsars. MSPs represent a smaller population of older pulsars. They are found throughout the Galaxy, probably less concentrated towards the plane than are the younger pulsars; many are also found to be located in globular clusters.

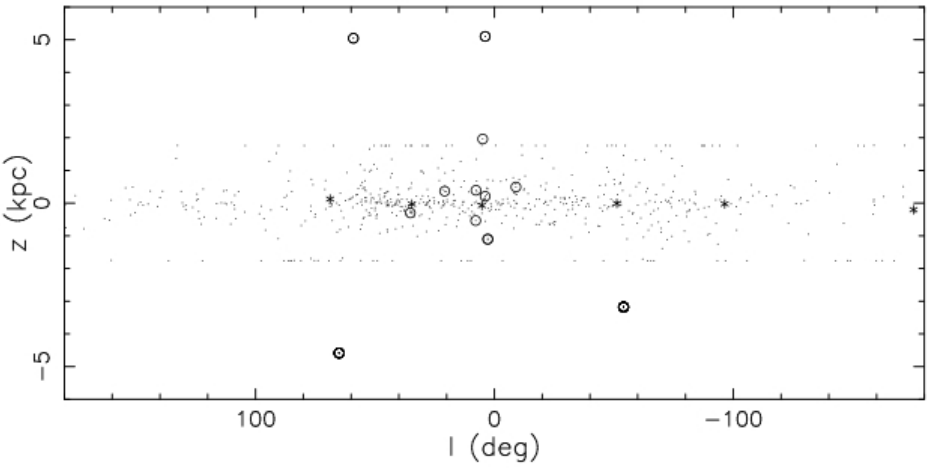

Figure 2.6: The distribution of radio pulsars in our galaxy, as found from distance determinations with use of the dispersion measure. Symbols ⊙ indicate pulsars in globular clusters, for which the distance is determined optically. (Credit: Frank Verbunt and John Heise, Astronomical Institute Utrecht)

2.6 Pulsar timing

The detected signal can be sampled and digitized at an arbitrary rate, and an arbitrary length of record can be searched by computer for the periodic signal. The principle of the search may be to look either directly for regular spaced pulses (a periodogram analysis) or for their spectrum within the Fourier transform of the data stream. The two approaches are closely related, but the Fourier transform method is used in all modern searches because it is more economical of computer resources. The Fourier analysis approach involves taking the Fourier transform of the time series and inspecting the resultant spectrum for fundamental-frequency signals together with any associated harmonics. The amplitude and phases of the individual harmonics are determined by the average pulse profile in the time domain. For a nearly sinusoidal pulse there will be a large fundamental spectral feature with small harmonics, while for a narrow pulse width W there will be approximately $P/2W$ harmonics with amplitude comparable to the fundamental. Individually these components may not be distinguishable from noise, and they must be combined in some way to maximize the detectability of the signal.

Although it is now accepted that most neutron stars are born in supernova explosions, only a small number of the known pulsars are clearly associated with visible supernova remnants. This is, of course, entirely consistent with the difference between the lifetimes of a typical pulsar (about $10^6 - 10^7$ years) and a supernova remnant (about $10^4 - 10^5$ years). Furthermore, most of these associated pulsars are obviously young, as seen from their large period derivatives $\dot{P}$. Their characteristic ages, $P/2\dot{P}$, are in sharp contrast with

those of the other short-period pulsars, the millisecond pulsars; these have very small period derivatives, are much older and are the product of a long evolutionary history.

The characteristic age of a pulsar, which is derived from its present-day rate of slowdown, is an unreliable indicator of its actual age since birth. Not only is it unsafe to assume that the rate of rotation at birth was much larger than at present but also the slowdown itself may change during the lifetime of the pulsar. Labeling a pulsar as young is only secure for the small number actually identifiable with datable supernovae. The prime example is the Crab pulsar.

Hewish and his collaborators, in the discovery paper of 1968 (Hewish et al. 1968), showed that the shortness of the pulses, and their precise periodicity, implied that the source was small and that it might be a rotating neutron star. They showed also that the arrival time was varying because of the Doppler effect of the Earth's motion around the Sun; this annual variation implied that the source laid outside the Solar System. Finally, they showed that the arrival time of a single pulse depended on the radio frequency; this dispersion effect was found to be in accord with the effect of a long journey through the ionized gas of interstellar space. Pulses from a pulsar lying in the plane of the ecliptic will therefore arrive earlier at the Earth than at the Sun when the Earth is closest to the pulsar. Assuming for simplicity that the Earth's orbit is circular and centered on the Sun, the delay is given by

$$t_c = A\cos(\omega t - \lambda)\cos\beta, \tag{2.13}$$

where A is the light travel time from Sun to Earth, ω is the angular velocity of the Earth in its orbit and λ, β are the ecliptic longitude and latitude of the pulsar. The observed arrival times of pulses emitted by a pulsar at equal time intervals throughout the year will therefore show a sinusoidal variation. The angular accuracy of the positions so determined is greatest near the pole of the ecliptic, since the ecliptic latitude β is poorly determined near $\beta = 0$. An error in the assumed coordinates gives rise to periodic timing errors:

$$\delta t_c = +A\delta\lambda \sin(\omega t - \lambda)\cos\beta - A\delta\beta\cos(\omega t - \lambda)\sin\beta. \tag{2.14}$$

Fitting such a model to the variation of pulse arrival times through a year gives positions that are remarkably accurate.

The task is to apply corrections to the observed times of arrival (TOAs) of pulses in order to give the times that would have been observed at the barycenter of the Solar System, so that they do not have the modulating effects arising from the Earth's motion. The components of the correction of pulse arrival times t to barycentric times t_b are:

$$t_b = t + \frac{DM}{\nu^2} + \Delta_R + \Delta_E + \Delta_S \tag{2.15}$$

Here DM/ν^2 is the dispersive propagation delay at radio frequency ν; Δ_R is a large geometrical term, which incorporates the classical geometry of the Solar System; Δ_E is the Einstein delay, due to gravitational redshift and time dilation; and Δ_S is the Shapiro delay, due to the curvature of space-time in the Solar System.

The analysis of the Roemer delay and the effects of general relativity allow the observed times of arrival to be reduced to a time of arrival at the barycenter of the Solar System. Starting at a reference time t_0, the expected pulse number N at an observed arrival time t is expressed as a Taylor series:

$$N = \nu_0(t - t_0) + \frac{1}{2}\dot{\nu}(t - t_0)^2 + \frac{1}{6}\ddot{\nu}(t - t_0)^3 + ... \tag{2.16}$$

The differences between the observed and calculated values of N are usually expressed as differences in arrival times, known as timing residuals.

On a time scale of some days, all pulsars show a remarkable uniformity of rotation rate: uniform rotation is exactly what is expected of a spinning body with a large stable moment of inertia and isolated in space.

Chapter 3

AQUEYE and IQUEYE

Astronomy is greatly advanced in terms of observational instruments. However, most astronomical instrumentation does not allow to directly distinguish the physical processes of the radiation source emission. As shown by Glauber (1963a), beyond the first-order coherence, higher-order coherence of light may in principle convey information about the physics of light emission or propagation. Such higher-order coherence of light can be measured from the arrival time statistics of individual photons. To quantify the amount of order in the photon stream arrival time, second and higher order coherence of light have to be measured over timescales comparable to the first order coherence time. For astronomically passbands ($\Delta\lambda \sim 1$ nm), the time required to detect second order effects is of the order of picoseconds (Dravins et al. 2005b). On the more realistic nanosecond scales, the effects are diluted but still measurable, as demonstrated years ago by Hanbury Brown (1974).

To explore the possibility of pushing the time resolution and time tagging capabilities of astronomical instruments beyond their current capabil-

ities, a conceptual study was carried out in the frame of the ESO 100 m OverWhelmingly Large Telescope (OWL) and of the ESO 42 m Extremely Large Telescope (E-ELT). The solution was called Quanteye (Dravins et al. 2005b). Quanteye can go into the domains of nanoseconds and beyond, sustaining GHz photon count-rates, thus approaching the realm of quantum optics with the capability to examine quantum statistics of photon arrival times. Quanteye on OWL is designed for the study of all the phenomena considered as high-speed astrophysics. But the aim of this instrument is to reach timescales sufficiently short to reveal the quantum-optical statistics of photon arrival times (Hanbury Brown 1974).

Since both OWL and E-ELT are still several years in the future, two prototypes were built to acquire experience: Aqueye, for the Asiago 1.8 m telescope (section 3.3), and Iqueye, for the 3.5 m New Technology Telescope of ESO in La Silla (section 3.1). Both instruments were used mainly to observe optical pulsars. Optical observations of pulsars not only add an important piece to the picture of their multiwavelength phenomenology but also play a major role in studying the intrinsic properties of neutron stars, from the structure and composition of the interior to the properties of the atmosphere and of the magnetosphere. In this chapter the two prototypes are described analyzing their performances and some of their results.

3.1 The Iqueye Single Photon Counting Photometer

Iqueye (Naletto et al. 2009) has been conceived as a precursor to a quantum photometer for the future 42 m European Extremely Large Telescope E-ELT (see Dravins et al. (2005b)), aiming to perform not only high speed photometry but also the measurements of the statistics in the photon arrival times and intensity interferometry (Hanbury Brown 1974). Iqueye is a conceptually simple fixed-aperture photometer which collects the light within a field of view (FOV) of few arcseconds around the target object. It is mounted at the Nasmyth focus of the 3.5 m ESO New Technology Telescope (NTT) in La Silla (Chile).

A holed folding mirror at 45° on the NTT focal plane brings a 1 arcmin field around the star under investigation to the field acquisition TV camera. The light from the target object instead passes through the central hole and is collected by a collimating refracting system. Two filter wheels located in the parallel beam after the first lens allow the selection of different filters and polarizers. The light then reaches a focusing system which (de)magnifies the telescope image by a 1/3.25 factor. On this intermediate focal plane, one out of three pinholes (200, 300 and 500 micrometers diameter) can be inserted. These pinholes act as field stops, and their sizes allow the selection of three different FOVs (3.5, 5.2 and 8.7 arcsec diameter). After the pinhole, the light impinges on a pyramid having four reflecting surfaces and whose tip coincides with the center of the shadow of the secondary mirror. The pyramid splits the telescope pupil in four equal portions, and sends the light from each sub-

Figure 3.1: Iqueye being mounted at the NTT in La Silla (Credit: Naletto).

pupil along four perpendicular arms (see Figure 3.2). Along each arm, the sub-pupil light is first collimated and then refocused by a suitable system, further (de)magnifying the image by an additional 1/3.5 factor.

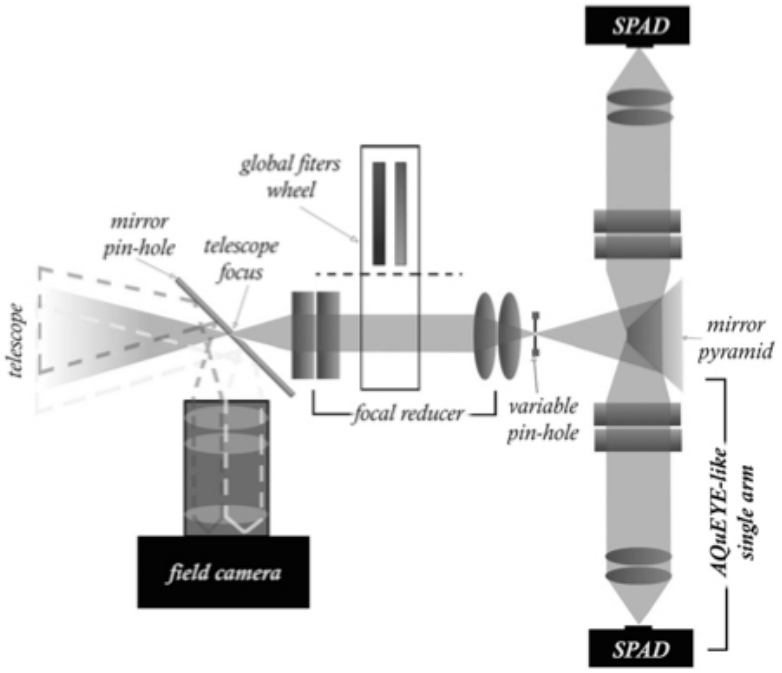

Figure 3.2: Schematic view of Iqueye optical design (Naletto et al. 2009).

Each sub-beam is then focused on a single photon avalanche photodiode (SPAD) operated in Geiger mode. The quantum efficiency of the Silicon SPADs extends from the blue to the near infrared, with a peak sensitivity of 55% at 550 nm. When used without filter, as in the present case, the overall efficiency of Iqueye (SPAD + telescope + atmosphere) at the Zenith is approximately 33%. The dark counts of the temperature-controlled detectors are very low, varying from 30 to 50 count/s for each individual unit. The

SPAD circular sensitive area of 100 μm diameter, nominally defines a 5.8 arcsec FOV. Therefore, the smallest pinhole acts as the actual field stop at 3.4 arcsec. This pinhole can be selected when it is necessary to reduce as much as possible the background around the target, e.g. when observing a pulsar embedded in a nebula, as in the present case. The main characteristics and performance of Iqueye are summarized in Table 3.1.

The optical solution of splitting the beam by a pyramid in 4 sub-beams was dictated by the need to overcome as much as possible the dead time intrinsic to the SPAD (75 nanoseconds), in order to give to Iqueye the largest possible dynamic range. In other scientific applications (e.g. intensity interferometry), having four independent detectors allows to cross correlate the counts from each sub-aperture.

System sensitivity	Photon counting
Relative time accuracy	100 ps (for 1 h of continuous observation)
Absolute time accuracy	500 ps (for 1 h of continuous observation)
Dark count rate	$<$100 Hz
Maximum count rate	8 MHz
Dynamic range	$>$40 dB
Limiting magnitude	$m_V = 24$ (with 2h exposure time and $S/N = 10$
Effective field of view	(selectable) 3.5, 5.2, or 8.7 arcsec
Operative spectral range	$\Delta\lambda$=[350,925] nm
System total efficiency	33% (peak @ 550 nm)
	18% (average over $\Delta\lambda$=[350,925] nm spectral range)

Table 3.1: Main characteristics describing the performance of Iqueye applied to NTT (Naletto et al. 2009).

The pulses produced by the SPADs, which have an intrinsic time jitter of the order of 35 ps, are sent to a CAEN (Costruzioni Apparecchiature Elettroniche Nucleari S.p.A., Italy) Time to Digital Converter (TDC) board

Long (°)	Lat (°)	Elevation (m)	X (m)	Y (m)	Z (m)
-70.733746	-29.258913	2424.09	+1838193.1	-5258983.2	-3100153.8

Table 3.2: Geodetic and geocentric Cartesian coordinates of the NTT (top of the roof, doors open, dome still)

which has a nominal resolution of 24.4 ps. Considering also the other possible noise sources, the nominal accuracy of the photon arrival time determination is of the order of 100 ps or better. An external Rubidium oscillator provides the reference frequency to the TDC board. The board acquires also a pulse-per-second (PPS) from a GPS receiver, used to remove the Rubidium frequency drift and to put the internal detection times on the UTC scale. Taking into account all error factors, the final overall precision of each time tag in the UTC scale is approximately 450 ps, maintained throughout the duration of the observations. In order to take care as well as feasible of the rotation of the NTT building, the GPS antenna was mounted on the top of the dome, at the centre of one of the sliding doors (about 3 meters away from the dome rotation axis). The signal was brought to the receiver by a high-quality, length compensated cable. The geodetic and geocentric Cartesian coordinates of the antenna, in the WGS94 reference system, are given in Table 3.2. These coordinates have been translated to the intersection of the optical and elevation axes using the construction drawings of the enclosure; taking into account the rotation, the actual precision is estimated better than 2 meters.

The user interface, developed as a Java multitasking code, controls each subsystem (e.g. the mechanisms), performs the data acquisition and storage,

provides some real time monitoring of the data acquisition, and provides tools for a quick look statistical analysis of the data. Each arrival time is recorded on the storage device which has a total capacity of approximately 2 TB. Being the data stored in a mass memory device, all the data can be analyzed in post-processing: this allows, for example, to sort the collected time tags in arbitrarily long time bins still preserving the original data (see Figure 3.3).

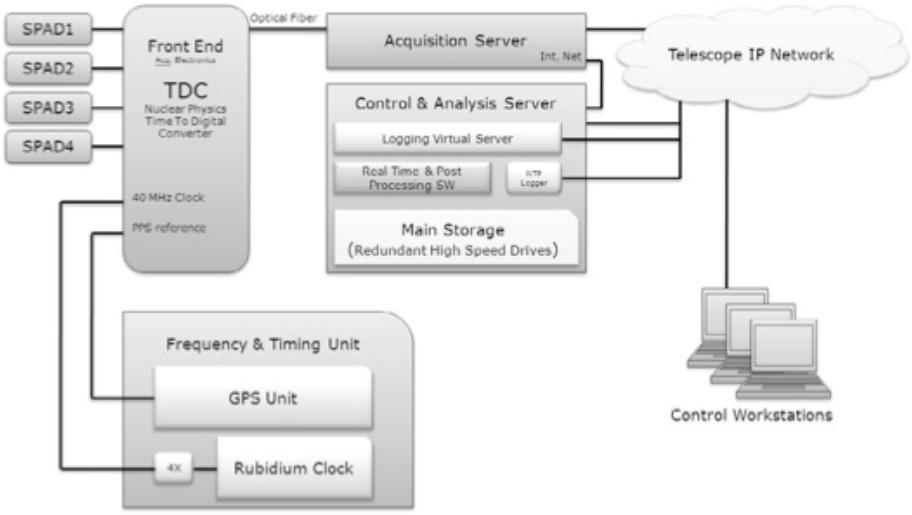

Figure 3.3: Conceptual schematic of the acquisition and timing system of Iqueye (Naletto et al. 2009).

In 2009, some improvements were made to the original instrument (Barbieri et al. 2010; Naletto et al. 2010), in particular the addition of a fifth SPAD to acquire the signal from the sky.

3.2 Iqueye's performance

To plan better astronomical observations and to fully express the technical quality of Iqueye, it is important to estimate the theoretical performance of the instrument, taking account, in particular, the environment in which it has to operate. This needs to be done not only to evaluate the quality of actual data but also to understand the capacity of Iqueye to study optical pulsars.

The most important quantities to consider are: the efficiency spectrum of Iqueye, the sky spectrum and the spectrum of the studied stellar object.

The global efficiency of Iqueye (Figure 3.4) has been estimated (Naletto et al. 2009) by taking into account the three reflections of NTT mirrors, the reflection at the pyramid, the nominal transmission of all the lenses, and the detector quantum efficiency. The global efficiency spectrum can be

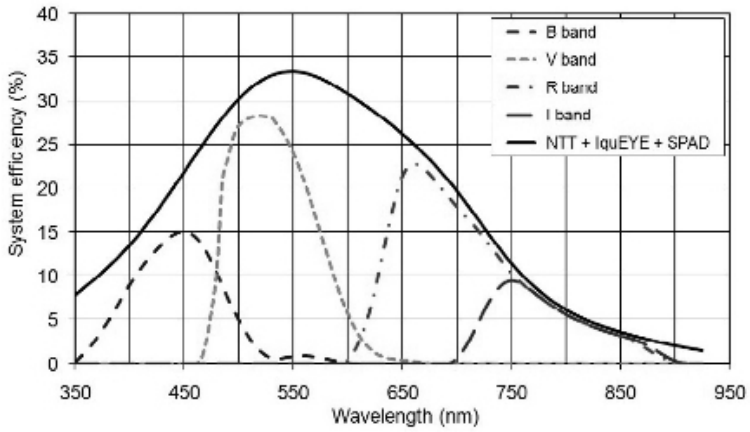

Figure 3.4: Estimated global efficiency (upper line) of Iqueye applied to NTT (Naletto et al. 2009).

1	2	3	4	5	6	7	8	9
U	0.365	8.2×10^{14}	0.068	4.2×10^{-8}	1.88×10^{-23}	22	150	10
B	0.44	6.8×10^{14}	0.098	7.2×10^{-8}	4.64×10^{-23}	23	100	10
V	0.55	5.5×10^{14}	0.089	4.0×10^{-8}	3.95×10^{-23}	22	170	15
R	0.70	4.3×10^{14}	0.22	1.8×10^{-8}	2.87×10^{-23}	21	250	55
I	0.90	3.3×10^{14}	0.24	8.3×10^{-9}	2.24×10^{-23}	18.5	1.5×10^{3}	370
J	1.25	2.4×10^{14}	0.28	3.07×10^{-9}	1.60×10^{-23}	16	1.0×10^{4}	2.8×10^{3}
H	1.65	1.8×10^{14}	0.30	1.12×10^{-9}	1.02×10^{-23}	13	5.6×10^{4}	1.7×10^{4}
K	2.2	1.4×10^{14}	0.42	4.07×10^{-10}	6.57×10^{-24}	12.5	4.4×10^{4}	1.8×10^{4}
L	3.45	8.7×10^{14}	0.60	7.30×10^{-11}	2.90×10^{-24}	5.5	8.0×10^{6}	5.0×10^{6}
M	4.7	6.4×10^{14}	0.67	2.12×10^{-11}	1.63×10^{-24}	2	1.0×10^{8}	7.0×10^{7}
N	10.2	2.9×10^{14}	5.2	1.10×10^{-12}	3.90×10^{-25}	-3	1.0×10^{9}	5.0×10^{9}
Q	20.0	1.5×10^{14}	5.2	7.80×10^{-14}	1.04×10^{-25}	-5	6.0×10^{8}	3.0×10^{9}

Table 3.3: The intensity of the sky background in the optical and infrared wavebands (Longair 2010). 1) Name of waveband; 2) Effective wavelength of the waveband (λ_{eff}/μm); 3) Effective frequency of the waveband (ν_{eff}/Hz); 4) Effective width of the band ($\Delta\lambda_{eff}/\mu$m); 5) Flux density of a zero magnitude star per unit wavelength ($S_\lambda(0)$/W/m^2/μm); 6) Flux density of a zero magnitude star per unit frequency range ($S_\nu(0)$/W/m^2/Hz); 7) Background intensity in magnitudes (arcsec^{-2}); 8) Background photon intensity per unit waveband (I(λ)/photons/m^2/arcsec^2/s/μm); 9) Background photon intensity in standard waveband given in column 4 (I/photons/m^2/arcsec^2/s).

approximated with the following polynomial:

$$y = -161.86\,x^5 + 543.44\,x^4 - 701.71\,x^3 + 431.24\,x^2 - 124.99\,x + 13.79$$

where x is the wavelength (μm) and y is the efficiency (in percentage).

The spectrum of the sky in La Silla was obtained starting from the values (Table 3.3) of the intensity of the sky background reported in Longair (2010), scaled by the values of the magnitude of the La Silla sky (Table 3.4).

It is possible to approximate the sky spectrum with the following poly-

	U	B	V	R	I
mag	21.9	22.7	21.9	21.1	19.9

Table 3.4: Magnitudes of the sky in La Silla (Chile).

nomial:

$$y = 16289\,x^3 - 21752\,x^2 + 9557.2\,x - 1251.9$$

where x is the effective wavelength of the waveband (λ_{eff}/μm) and y is the photon intensity per unit waveband (I(λ)/ph/m^2/arcsec^2/s/mum).

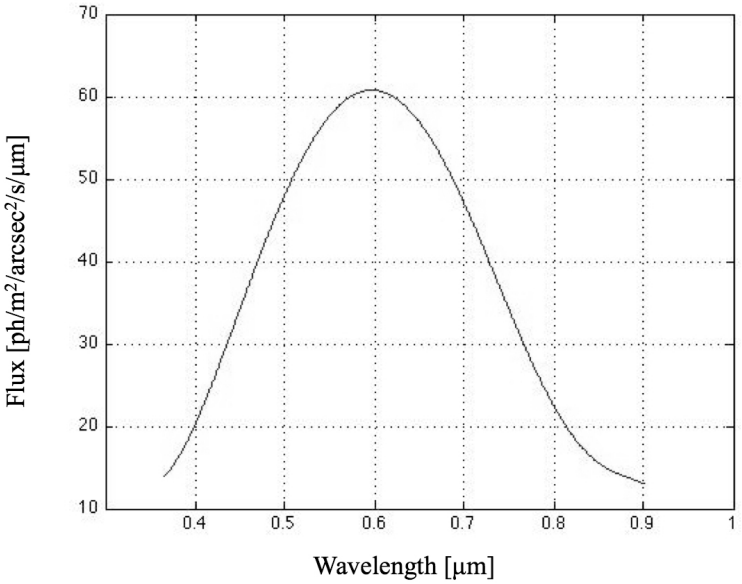

Figure 3.5: La Silla sky spectrum combined with Iqueye efficiency.

Combining the spectrum of the sky with the efficiency of the instrument (Figure 3.5) the theoretical sky flux was obtained:

$$F_{sky} = 20\,\text{photons/m}^2\text{/arcsec}^2\text{/s}. \tag{3.1}$$

Since the NTT telescope at La Silla has a diameter of 3.6 m, the sky flux is:

$$F_{sky} = 207 \text{ photons/arcsec}^2\text{/s}. \tag{3.2}$$

Since during the observations the dimension of the pinhole can be changed, it is important to take in account the differences in flux. We consider here just the two pinholes actually used during the observations, 3.5 arcsec and 5.2 arcsec:

$$F_{sky\,3.5} = 1988 \text{ photons/s} \tag{3.3}$$

$$F_{sky\,5.2} = 4390 \text{ photons/s} \tag{3.4}$$

3.2.1 Theoretical flux of B0540-69, Crab and Vela pulsars

Three optical pulsars were observed by Iqueye in 2009: Crab pulsar, PSR B0540-69 and Vela pulsar. In this thesis only the results obtained by the observation of PSR B0540-69 were fully analyzed (see chapter 4) but the examination of the performance of Iqueye was developed also for the Crab and Vela pulsars.

The spectrum of PSR B0540-69 in the optical, obtained by Mignani et al. 2010 (Figure 3.6), can be approximated by:

$$y_{B0540-69} = (2.4012 \times 10^{-15})\, x^3 - (3.3707 \times 10^{-12})\, x^2 + (2.055 \times 10^{-11})\, x + 1$$

where x is the frequency (THz) and y is the logarithm of the flux ($\log(\mu\text{Jy})$).

The estimated total flux is obtained combining the spectrum of PSR

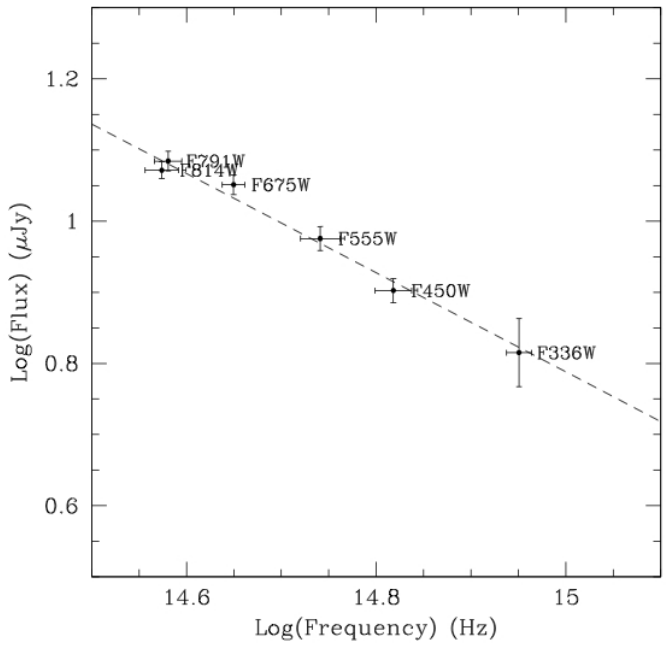

Figure 3.6: Mignani et al., 2010. Optical spectral energy distribution of PSR B0540-69 derived from the available multi-band WFPC2 photometry. Points are labelled according to the filter names. The dashed line is to the best fit power-law spectrum.

B0540-69 with the efficiency of the instrument (Fig. 3.7) and assuming we aren't using filters or polarizers:

$$F_{B0540-69} = 28 \text{ photons/m}^2\text{/s}. \tag{3.5}$$

Considering the telescope diameter, the resulting flux is:

$$F_{B0540-69} = 286 \text{ photons/s}. \tag{3.6}$$

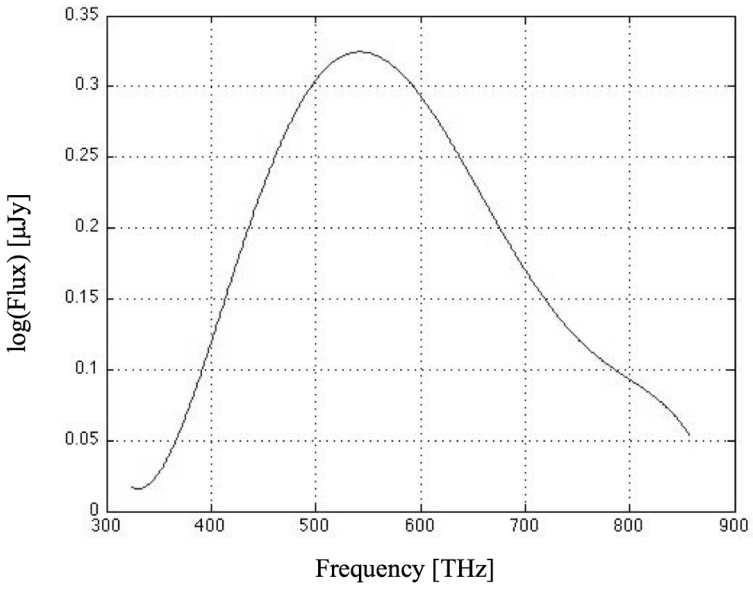

Figure 3.7: PSR B0540-69 spectrum combined with Iqueye efficiency.

To quantify the quality of this result, a confrontation with real data has been done. We will use the results of one night of Iqueye's observations of PSR B0540-69 performed in 2009: the observation of December 18, 2009,

has the better S/N ratio so we will use this night for the comparison. Table 3.5 shows the characteristics of the observation and the number of detected photons versus the expected photons: it is possible to see that the results are in good agreement. This confirms the good quality of the observation and also set a method to evaluate future similar observations.

Observation duration (s)	Pinhole	Detected photons	Expected photons
3600	3.5	8 304 630	8 184 154

Table 3.5: Comparison between real detected photons and theoretically expected photons in the Iqueye's observation of PSR B0540-69 (December 18, 2009).

As previously said, a similar analysis was done also for the Crab and Vela pulsar, combining their spectra (derived from the spectral flux distribution shown in Figure 3.8) with the efficiency of Iqueye (Fig. 3.9 and 3.10) and obtaining the following results:

$$F_{Crab} = 88695 \text{ photons/s} \tag{3.7}$$

$$F_{Vela} = 41 \text{ photons/s}. \tag{3.8}$$

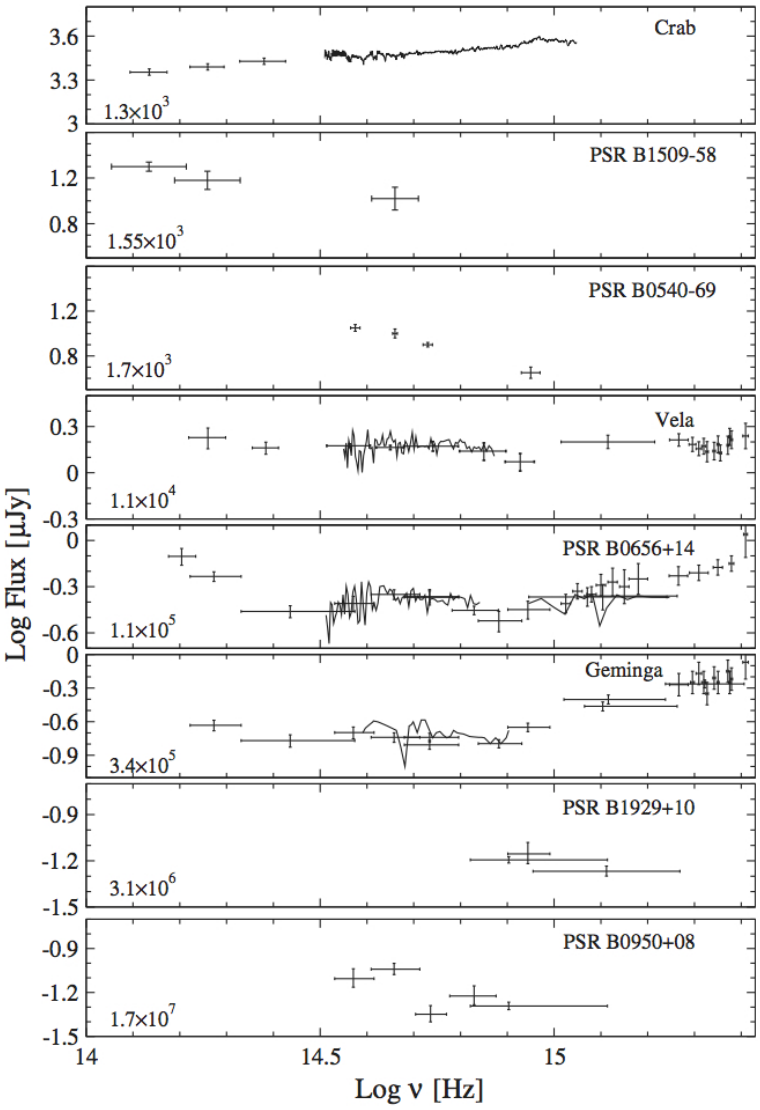

Figure 3.8: Spectral flux distribution of all rotation-powered pulsars for which either medium-resolution spectroscopy or multi-band photometry is available. From top to bottom, objects are sorted according to increasing spin-down age. (Mignani et al. 2007).

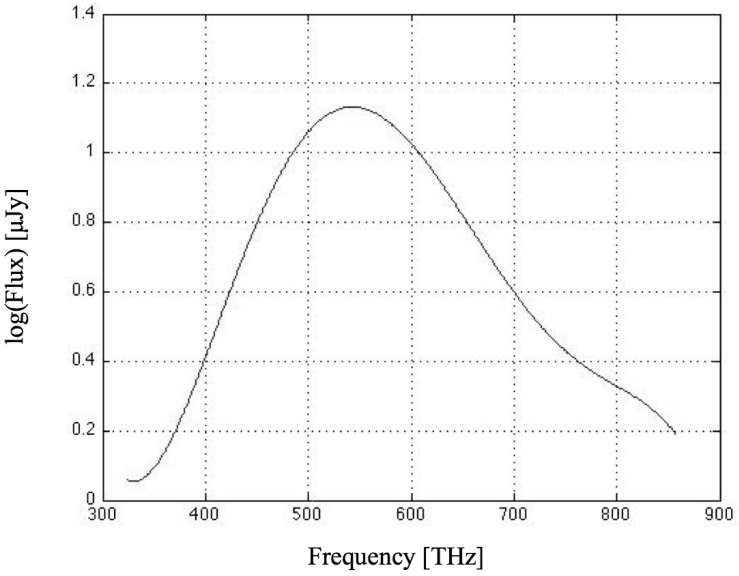

Figure 3.9: Crab pulsar spectrum combined with Iqueye efficiency.

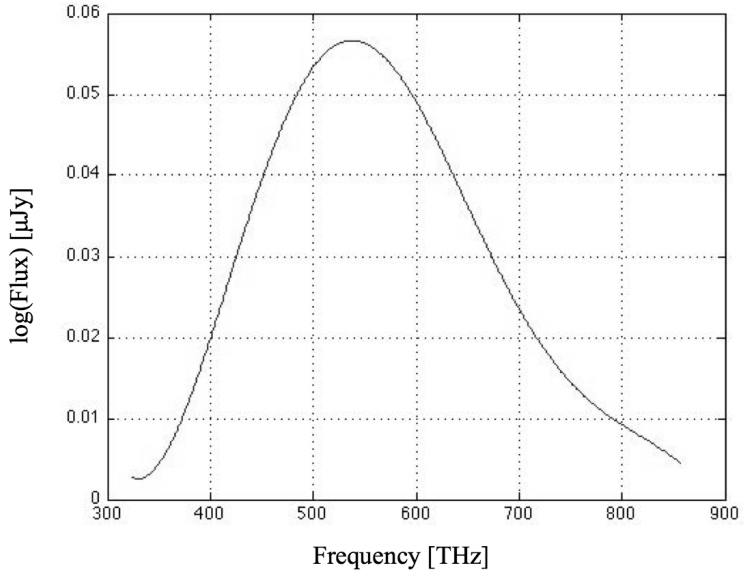

Figure 3.10: Vela pulsar spectrum combined with Iqueye efficiency.

3.3 The Asiago Quantum Eye

Before Iqueye, the first prototype of an ultra-fast photometer was Aqueye (Asiago Quantum Eye). Even if the main focus of this thesis is on Iqueye, here we want to briefly illustrate some of the results obtained with Aqueye in order to underline the quality of the project that lies at the bottom of the conception of these instruments.

Built for the 182 cm Copernico Telescope at Cima Ekar (Asiago, Italy), Aqueye works in a way similar to Iqueye: it isolates a single object at the center of the telescope field of view and divides the telescope pupil in four parts. Each sub-pupil is then focused on a SPAD capable to tag the arrival time of each photon to better than 50 picoseconds (Barbieri et al. 2007).
A way to realize this prototype was by dividing the telescope pupil in four parts by mounting a pyramidal mirror at the exit of AFOSC, the Asiago Faint Object Spectrograph and Camera (Figure 3.11). AFOSC is mounted on a flange which takes care of many observational needs, from pointing and guiding to field vision and rotation. Different filters and polarizers can be inserted in the parallel beam section, giving the capability to define four independent photometers (Figure 3.12).

The optical performance of the designed system is excellent over the 50 micron detector area, insuring an energy concentration from the blue (420 nm) to the red (700 nm) better than 90%. In order to take into account the average seeing conditions at the Asiago 182 cm telescope, the field of view has been increased to 3 arc seconds. The Aqueye mechanical design is shown in Figure 3.13.

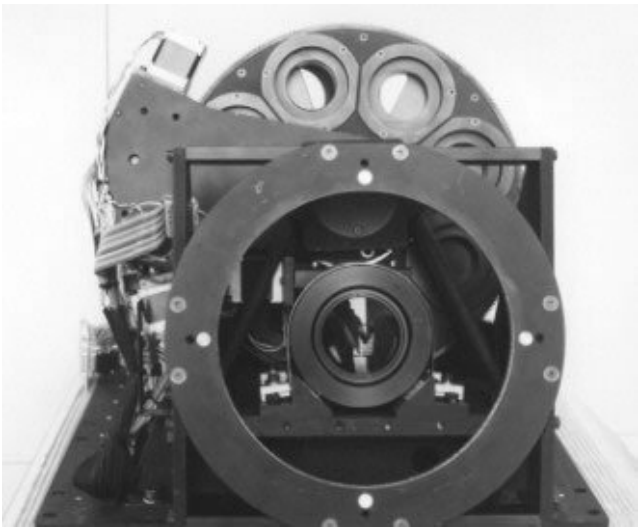

Figure 3.11: AFOSC seen from the CCD point of view (http://www.oapd.inaf.it/asiago/).

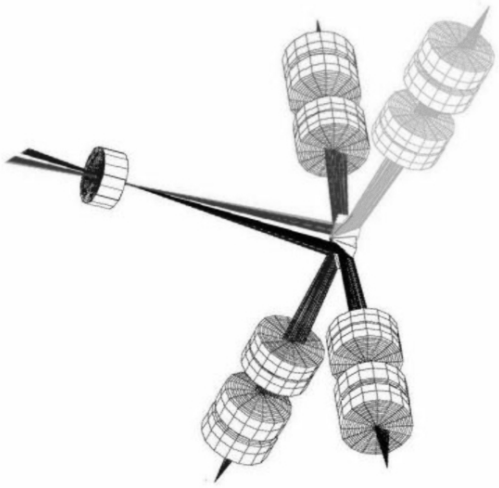

Figure 3.12: Following the last lens of AFOSC, an aluminized pyramid splits the light into four separate channels imaged to each SPAD (Barbieri et al. 2007).

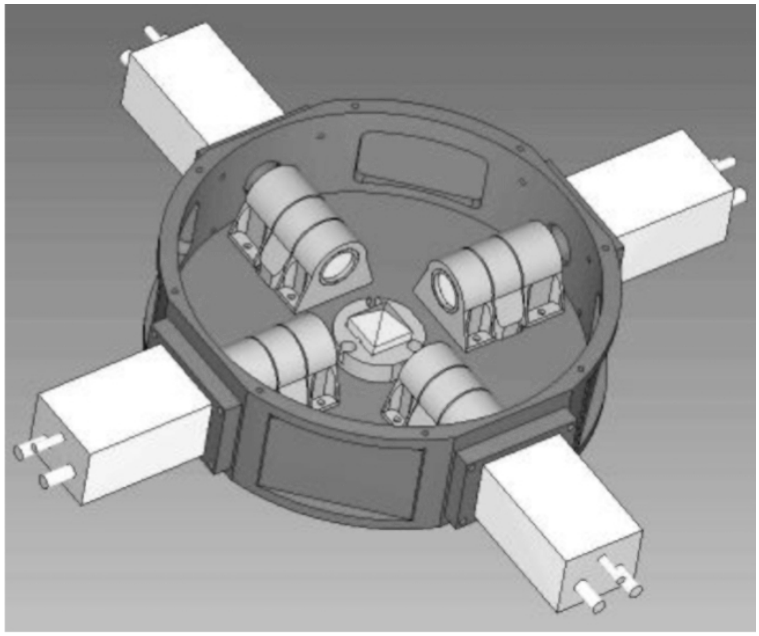

Figure 3.13: The mechanical design of Aqueye (Barbieri et al. 2007).

As for Iqueye, the core of the electronics system is a CAEN TDC board, able to tag each event with a time precision of 35 ps per channel. It makes use of an external Rubidium oscillator as external reference frequency. To generate and maintain a very accurate time for hours, the start/stop commands are tied to the UTC by means of the GPS signal. In this way, the data can refer to a common time scale adopted by all telescopes on the ground or in space.

3.3.1 Optical observations of the Crab pulsar

Since its discovery (Staelin & Reifenstein 1968), the pulsar in the Crab nebula has been one of the most targeted objects in the sky at all wavelengths. The optical light curve of the Crab pulsar has been monitored through the years using a variety of telescopes and instruments (Słowikowska et al. 2009). The pulse shape is characterized by a double peak profile, separated in phase by $\sim 140°$, and it is similar through the entire electromagnetic spectrum.

The Crab pulsar was observed with Aqueye mounted at the 182 cm Copernico Telescope in Asiago (Zampieri et al. 2011; Germaná et al. 2011). The observations were performed in 2008 and lasted for three nights, starting from October 10 (see Table 2.6). The adopted position of the Crab pulsar is that reported in the Jodrell Bank monthly ephemerides (R.A. 05h 34m 31.97232s, DEC. $+22°\ 00'\ 52.0690''$ [J2000]), with no correction for proper motion.

During each observing run, the arrival time of $\sim 0.5 - 2 \times 10^7$ photons has been recorded, time-tagged with a relative time accuracy of ~ 100 ps and an

	Starting time (UTC)	Duration (s)
1	October 10, 23:45:15	1078
2	October 11, 00:05:08	1197
3	October 11, 01:00:23	1797
4	October 11, 01:45:45	1797
5	October 11, 02:23:08	1631
6	October 11, 03:23:47	1197
7	October 11, 23:25:09	3597
8	October 12, 23:13:58	3998

Table 3.6: Log of October 2008 Crab pulsar observations performed with Aqueye. The start time of the observations is the GPS integer second, accurate to better than approximately ±30 ns (Germaná et al. 2011).

absolute precision (referred to UTC) better than 500 ps. To our knowledge, this is the most accurate arrival time of photons from the Crab pulsar ever obtained in the optical band.

In Figure 3.14, the light curve of the Crab pulsar is shown, folded over the average spin period for one of the Aqueye observations: 11 October 2008, 01:45:44 UTC. The folded curve has 1000 bins in phase, with a resolution of ~ 33.6 μs. The light curve includes the contribution of both the pulsar and the nebular background entering the Aqueye pinhole entrance aperture. The average count rate of the Crab pulsar measured by Aqueye is ~ 5500 counts s^{-1}. The count rate of the background is ~ 4500 counts s^{-1}, which implies a total number of net source photons of $\sim 2.6 \times 10^6$.

For the observation shown in Figure 3.14 (observation 4 in Table 2.6), the period is $P = 0.0336216424$ s. For comparison, the period at mid observation obtained interpolating the radio Jodrell Bank Crab ephemerides is $P = 0.0336216423$ s. The difference with respect to our measured period is 0.1 ns. This can be considered as an estimate of our present uncertainty

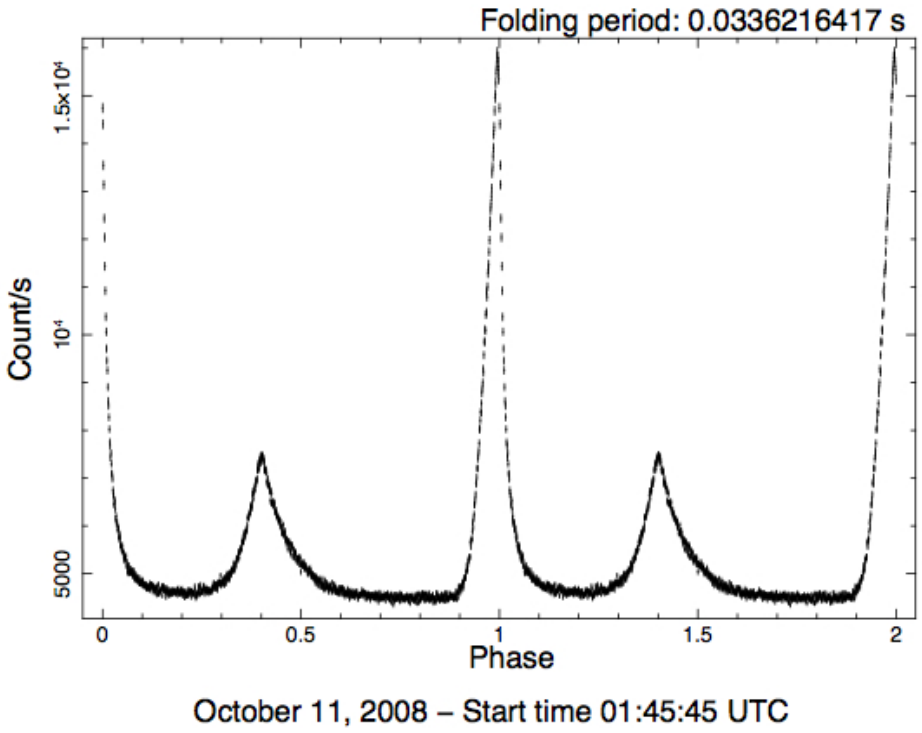

Figure 3.14: Folded light curve over the average period of the Crab pulsar for the Aqueye observation 4 in Table 2.6. Two rotations of the neutron star are shown (Germaná et al. 2011).

on the period measurement in a single observation with Aqueye. Fitting the measurements obtained during the nights of observation, an estimate of the period derivative can be obtained. Referring the period measurements to mid observation, at the barycentric corrected time $t_0 = 54749.0$ (MJD), the period and period derivative are $P = 0.033621602861 \pm 8.7 \times 10^{-11}$ s and $\dot{P} = (4.2061 \pm 0.0056) \times 10^{-13}$ s/s (2σ errors), within 0.06 ns and 0.005%, respectively, from the Jodrell Bank Crab ephemeris (Zampieri et al. 2011).

The data obtained by Aqueye allowed also a comparison between the phase of the Crab pulsar with that reported in the radio archive at the Jodrell Bank Observatory (Lyne et al. 1993). The time of arrival at the detector of the first pulse of the light curve after a certain reference epoch t_0 is $t_{arr} = (1 - \phi_0)P_{init}$, where $\phi_0 = \phi(t_0)$ is the phase of the main peak at t_0. Figure 3.15 shows the difference between the optical time of arrival of the main peak of the Crab pulsar and the radio one determined from the Jodrell Bank radio ephemerides. We found that the optical peak leads the radio one: the time difference is $\sim 113 \pm 61\,\mu$s at MJD = 54750 (Germaná et al. 2011). This result is in agreement with what was previously found by Shearer et al. (2003).

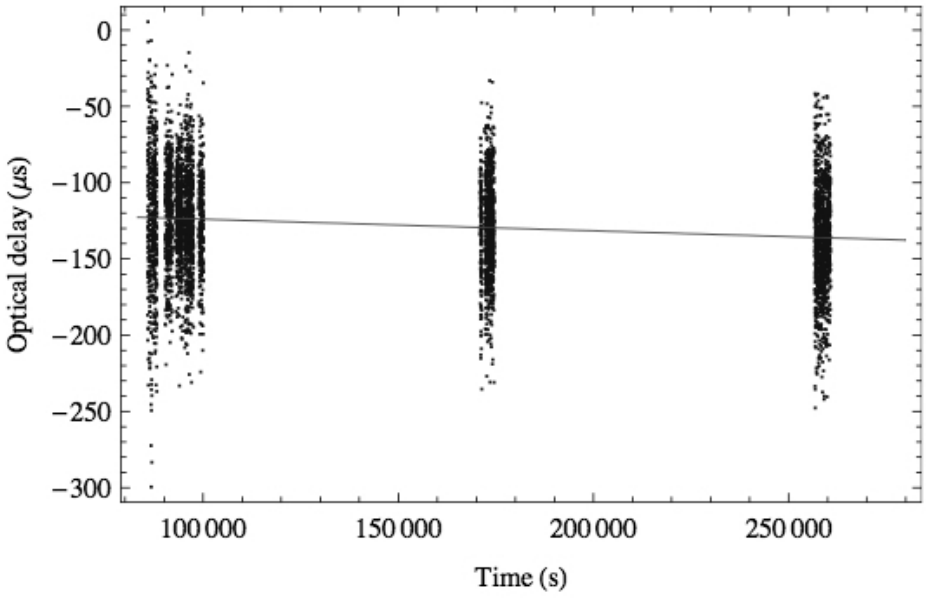

Figure 3.15: Difference between the optical and radio time of arrival of the main peak of the Crab pulsar. The negative value means that the optical peak leads the radio one by ~ 113 μs (Germaná et al. 2011).

Chapter 4

PSR B0540-69

With a period of about 50 ms and a characteristic age around 1670 years, PSR B0540-69 is often referred as the twin of the more famous Crab pulsar, since its rotational period, surface magnetic field, and spin down luminosity are similar to those of the Crab pulsar. While they have these similarities, the observed pulse profile are quite different to each other. The pulse profile of PSR B0540-69 consists of a single broad peak whereas the pulse profile of the Crab pulsar shows a sharp double-peak structure.

PSR B0540-69 is located in the Large Magellanic Cloud, at a distance d$\sim$ 49 kpc, and is therefore one of the most distant pulsars so far detected (Figure 4.1). It was discovered first in X-rays (Seward et al. 1984), later optically (Middleditch & Pennypacker 1985) and finally in radio (Manchester et al. 1993b). As in other young pulsars, the optical and X-rays profiles are similar (Plaa et al. 2003). Like the Crab pulsar, PSR B0540-69 is near the centre of a bright supernova remnant, although this is in turn at the centre of another shell-like nebula (Manchester et al. 1993b). The diameter of the

central component is 1.3 pc, comparable with the Crab Nebula (3.5×2.3 pc), and the shell nebula is 17.5 pc across.

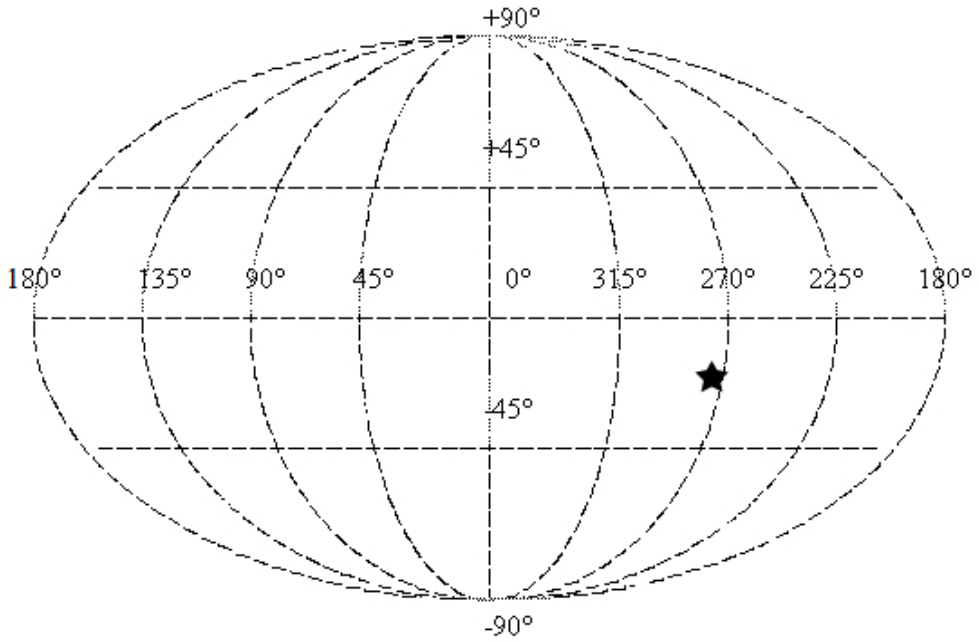

Figure 4.1: Location of PSR B0540-69 (black star) in galactic coordinates: Lon 279.7171, Lat -31.5157 (Livingstone et al. 2005).

4.1 The optical light curve of the LMC pulsar B0540-69 in 2009 (Gradari et al. 2011)

B0540-69 is the second brightest in the optical band after the Crab pulsar. It has been observed in recent years with a variety of imaging and spectroscopic instruments on ground telescopes (e.g. Mignani et al. (2010c); de Luca et al. (2007); Serafimovich et al. (2004); and references therein). However, the number of published optical light curves is fairly small, and all amount to data obtained more than 10 years ago. The first published light curve was obtained by Middleditch & Pennypacker (1985); Middleditch et al. (1987) using the 4-m and 1.5-m telescopes at Cerro Tololo. Then, Gouiffes et al. (1992) derived a second light curve from data taken with the ESO 3.6m telescope in the interval 1989 January 1991 April. Boyd et al. (1995) obtained a third light curve with the High Speed Photometer (HSP) on board the HST. All light within the HSP sensitivity band from 160 to 700 nm was used, observing the pulsar for one hour on August 26, 1993 through a $0''.65$ diaphragm. The sample time was 300 microseconds. The HSP light curve was consistent with the shape seen by Middleditch et al. (1987) and Gouiffes et al. (1992), and showed with greater clarity the double peak structure. The HSP light curve was compared to those obtained by several hard X-ray instruments by Plaa et al. (2003), who fitted the pulse shape with a double Gaussian curve. A fourth curve, from data obtained in May 1994 at the ESO 3.6m telescope, was inserted by Mignani et al. (1998) in a paper about the pulsar PSR B1509-58. Subsequently, Deeter et al. (1999) published a light curve based on data originally taken by Manchester & Peterson (1989) at

the 4-m Anglo Australian Telescope over the period 1986 14 July to 1988 16 June. Finally, Ulmer et al. (1999) published a light curve obtained at CTIO in Nov. 1996, and suspected a strong phase difference between optical and X-ray data. All those optical pulse shapes are broadly consistent with the radio one (Manchester et al. 1993a) and with those observed in the X- and Gamma-ray domains (e.g. Mineo et al. (1999a); Deeter et al. (1999); Plaa et al. (2003); Campana et al. (2008)).

We observed the pulsar at the ESO NTT with our very-high-speed photometer Iqueye (see Chapter 2) in January and December 2009. Our optical light curve is therefore the first derived from data acquired since 1996.

4.2 Observations and analysis

The observations were obtained through 3.5 or 5.2 arcsec diaphragms, without filters (maximum sensitivity around 550 nm, bandwidth at half maximum approximately 300 nm). The observation log is provided in Table 4.1. The columns UTC and MJD = Modified Julian Date = JD - 2 400 000.5 provide values of time and date at mid counting period referred to the barycentre of the solar system in TCB units (see later for the adopted procedure).

The procedure we routinely follow at the telescope to centre faint pulsating objects is to bin the arrival times in convenient time bins, e.g. 1/20 of the expected period, so that standard time-series analysis algorithms can be applied to single out the frequencies in the signal. After few minutes of trying in a given position, a slightly different one is tested until the position giving the best signal is found. Then, a long observation is started. In the

Date	UTC (hh mm ss)	MJD (d) (mid-exposure time)	Observation duration (s)	Diaphragm diameter (arcsec)
2009 01 18	05 11 10.0	54849.21665	5994	3.5
2009 01 20	04 03 19.0	54851.16190	5874	5.2
2009 12 14	07 27 59.9	55179.31111	3600	3.5
2009 12 15	02 42 00.0	55180.11250	3600	3.5
2009 12 16	01 39 59.6	55181.06944	3000	5.2
2009 12 18	02 30 00.3	55183.10417	3600	3.5

Table 4.1: Log of the observations of Iqueye at the NTT.

case of B0540-69, the procedure converged very quickly. The Power Spectral Density of the data was dominated by a frequency at the expected value of 19.7433 Hz (period around 0.05065 s) for January's data and 19.7380 Hz (period around 0.05066 s) for December's data with a statistical significance higher than 20 standard deviations (σ's) of noise; no other signal was visible above $3\sigma'$s of noise in the range 0-200 Hz. In December, this standard procedure was greatly helped by the availability of a very deep finding chart, kindly provided by Mignani et al. (2010c) (their fig. 1) before publication.

In order to perform the detailed analysis of the period and light curve, the arrival times of the photons are referred to the barycentre of the solar system, by using the latest release of the Tempo2 software (Hobbs et al. 2006) with the DE405 JPL Ephemerides (Standish 1998). The assumed celestial coordinates of the source are RA2000= 05h40m11s.202±0s.009; DEC2000 $= -69°19'54''.17 \pm 0''.05$ (Mignani et al. 2010c), with zero proper motion (Mignani et al. (2010c); de Luca et al. (2007)). These values have been measured on images taken with the HST/WFPC2 through the F555 and F547nm filters, and have been referred to the absolute reference frame using

astrometric data of the dense Two Micron All Sky Survey (2MASS) catalogue (Skrutskie et al. 2006). Therefore, the positions of Mignani et al. (2010c), (incidentally very close to the pointing used by Boyd et al. (1995)) are more accurate than those published by Serafimovich et al. (2004) and by Shearer et al. (1994).

The spin period, P, of the pulsar was determined by an epoch-folding technique similar to that expounded by Leahy et al. (1983). The spin period P was computed separately for each night, starting from the values given by Livingstone et al. (2005) and reported to our dates by means of the first and second derivatives. A 3 μs wide window of periods was analyzed with a sampling of 0.3 ns. For each of these 9000 trials, the data were initially binned in 20 phase bins, in order to be close to the procedure used by Boyd et al. (1995) with HST data. For each period, the χ^2 values against the zero hypothesis of a flat curve was calculated, obtaining a well defined distribution peaked around the expected value. The best period was then obtained through a least-squares fit of the χ^2 distribution with a Gaussian curve. The fit value of this Gaussian curve corresponds to the best fitting period, and the variance gives an indication of the dispersion of the period values. In Table 4.2 we report the results of the procedure, in terms of both the measured period P and the corresponding pulsar spin frequency ν. The quoted errors on P are the standard deviation on the mean value of the Gaussian curve fitted to the χ^2 distribution while those on ν are obtained by error propagation.

With our data alone, obtained over a time span of one year, we can determine the first derivative of the frequency. Using $t_0 = 55183.1042$ MJD as reference date in a linear fit, we obtain $\nu_0 = 19.7379712 \pm 4.83 \times 10^{-6}$ Hz

Date (MJD)	Period (s) and error (s)	Frequency (Hz) and error (Hz)
54849.21665	0.050 649 974 5 (0.30×10^{-9})	19.743 346 6 (0.12×10^{-6})
54851.16190	0.050 650 017 3 (0.25×10^{-9})	19.743 329 9 (0.09×10^{-6})
55179.31111	0.050 663 549 8 (0.32×10^{-9})	19.738 056 3 (0.13×10^{-6})
55180.11250	0.050 663 632 9 (0.26×10^{-9})	19.738 023 9 (0.10×10^{-6})
55181.06944	0.050 663 671 5 (0.38×10^{-9})	19.738 008 9 (0.15×10^{-6})
55183.10417	0.050 663 753 2 (0.27×10^{-9})	19.737 977 1 (0.11×10^{-6})

Table 4.2: Periods and frequencies of PSR B0540-69 determined with Iqueye data obtained during 2009.

and $\dot{\nu_0} = -1.86346 \times 10^{-10} \pm 2.65 \times 10^{-13}$ Hz/s. These values are in good agreement with those available in the literature as discussed at the end of the following Section.

The combined Iqueye light curve for all nights of January and December 2009 is shown in Figure 4.2 with phase resolved 50 bins and displayed for better visualization over two cycles. The curves pertaining to each night have been aligned in phase and then weighted for the respective χ^2 value. The phases of all curves have been fitted to the one of December 18 because of the better S/N ratio of those data.

The modulation M of our light curve, defined as

$$M = \frac{< c > - c_{min}}{< c >}, \tag{4.1}$$

where $< c >$ is the mean count rate in the pulse profile and c_{min} is the minimum count rate, is of the order of 1.5% for Iqueye, as for all ground telescopes. Therefore, all available light curves published over the last 27 years have approximately the same modulation, and broadly show the same

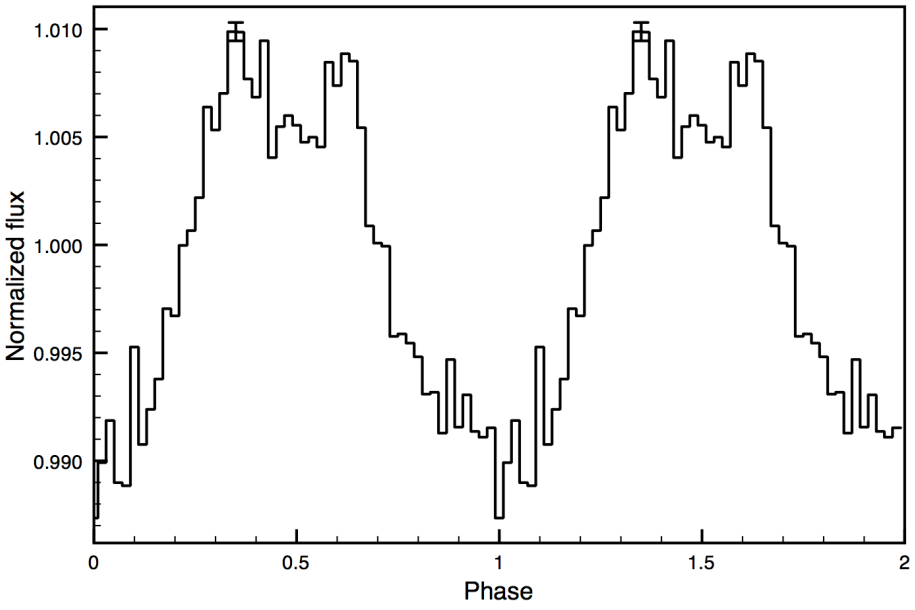

Figure 4.2: The overall Iqueye light curve in Jan and Dec 2009, from the individual curves weighted according to the respective χ^2 value and binned in 50 phase intervals. The counts have been normalized to the average count value during a period. For clarity the curve is shown over two cycles. The vertical bar shows the 1 sigma error. The phases of all curves have been fitted to the one of Dec. 18.

features, namely a main pulse with a total duty cycle of about 45% and complex structure. Given the high number of photons, and the extremely accurate time tagging guaranteed by Iqueye, we feel confident to say that the Iqueye light curve shown in Fig. 4.2 is the best available so far in visible light. The total duration of the main peak is approximately 22 ms (FWHM), with a central shallower feature suggesting the superposition of at least two peaks, as indicated also by the steeper slope of the ascending branch (0.062 ± 0.004 vs -0.046 ± 0.005 in units of normalized flux per phase unit) and already found by Plaa et al. (2003) from X-ray data. Therefore we have fitted the broad central peak with two Gaussian components separated by 0.25 (± 0.0098) in phase, the leading one approximately 1.0001 times higher than the second one, and with a FWHM of 17 ± 3.6 ms and 9.6 ± 0.9 ms respectively.

4.3 Discussion of the braking index and age

In commonly assumed models for pulsar spin-down, a braking index n and a characteristic age τ_c are defined (Livingstone et al. 2007) by:

$$\dot{\nu} = -K\nu^n, n = \frac{\nu\ddot{\nu}}{\dot{\nu}^2}, \tau_c = \frac{\nu}{2\dot{\nu}}, \tag{4.2}$$

where ν is the pulse frequency, $\dot{\nu}$ and $\ddot{\nu}$ are the first and second frequency derivatives respectively, and K is a constant. The braking index provides insight into the physics of the pulsar mechanism. Indeed, the actual value of the braking index is strictly related with the pulsar spin-down mechanism. It is well known (Manchester & Taylor 1977) that for magnetic dipole emis-

sion, as well as for the aligned rotator model of Goldreich & Julian (1969), $n = 3$. Different values of n would correspond to different processes of rotational energy loss and, in particular, values lower than 3 indicate that an additional torque is contributing to the spin-down. It should be noted that the value of n also affects the determination of the pulsar age, with $n < 3$ providing consistently larger values than those predicted by the characteristic age. Among the additional spin-down mechanisms, the distortion of the magnetic dipole geometry, a time variable magnetic field, a change with time of the inclination angle between rotation and magnetic axes, and/or the presence of particles/currents in the magnetosphere have been suggested (Ghosh 2007; Livingstone et al. 2007). As for the Crab pulsar, in the case of PSR B0540-69 the existence of a synchrotron-emitting nebula around the pulsar provides independent evidence for a particle wind originating from the pulsar magnetosphere, whose plasma may then contribute an additional spin-down torque (as suggested also by Boyd et al. (1995)). However, precisely determining what physical mechanism is responsible for the observed braking index of PSR B0540-69 and pulsars in general remains a completely open question. Unfortunately, the measurement of the braking index n is a difficult task, and only the youngest pulsars (typical ages less than 2 kyears) possess all needed qualities, in particular rapid spin-down and small relatively infrequent glitches. As an example, a braking index $n = 2.51 \pm 0.01$ has been measured for the Crab pulsar. PSR B0540-69 bears many similarities to the Crab pulsar, like period- and magnetic- field strength (50 vs 30 ms, 5×10^{12} G vs 4×10^{12} G, see Campana et al. (2008)), but its much larger distance prevents regular radio observations, and conflicting values of

n are reported in the literature. Livingstone et al. (2005) compared many of these different values, and finally concluded that the best estimate for the braking index is $n = 2.140 \pm 0.009$. The optical data available until our observations provided the following values: Manchester & Peterson (1989), $n = 2.01 \pm 0.02$, Gouiffes et al. (1992), $n = 2.04 \pm 0.02$, and Boyd et al. (1995), $n = 2.28 \pm 0.02$. We calculated the first and second frequency derivatives adding the frequency values measured with Iqueye in January and December 2009 to the previously published data sets. The frequency values considered for our analysis are summarized in Table 4.3. We have taken into account only measured, i.e. not interpolated, values, covering the entire spectrum from radio to X-ray at different dates. These values have been fitted with a second order polynomial (Figure 4.3), using least-squares regression, in the assumption of none or very small and infrequent glitches:

$$\nu(t) = \nu(t_0) + \dot{\nu}(t - t_0) + \frac{1}{2}\ddot{\nu}(t - t_0)^2. \tag{4.3}$$

The coefficients of the best fitting parabola, where t_0 is the value of the central date, are reported in Table 4.3.

With the so determined values of t_0, ν_0, $\dot{\nu_0}$ and $\ddot{\nu_0}$, the resulting value for the braking index is

$$n = 2.080 \pm 0.015 \tag{4.4}$$

and the characteristic age is

$$\tau = 1677.5\,\text{years}. \tag{4.5}$$

MJD	Frequency (Hz)	Band	Ref.
44186.91740	19.91687532	X	Seward et al. (1984)
45940.86590	19.88811520	VIS	Middleditch & Pennypacker (1985)
46111.07682	19.88533133	VIS	Middleditch et al. (1987)
49225.25570	19.83449650	HST (UV+VIS)	Boyd et al. (1995)
51421.62400	19.79880010	X	Kaaret et al. (2001)
52857.86600	19.77553000	X	Johnston et al. (2004)
53761.76200	19.76092260	X	Campana et al. (2008)
53843.56100	19.75959520	X	Campana et al. (2008)
54849.21665	19.74334657	VIS (Iqueye)	Gradari et al. (2011)
54851.16190	19.74332988	VIS (Iqueye)	Gradari et al. (2011)
55179.31111	19.73805633	VIS (Iqueye)	Gradari et al. (2011)
55180.11250	19.73802395	VIS (Iqueye)	Gradari et al. (2011)
55181.06944	19.73800890	VIS (Iqueye)	Gradari et al. (2011)
55183.10417	19.73797709	VIS (Iqueye)	Gradari et al. (2011)

Table 4.3: Frequencies used for the calculation of the braking index. Values are taken from the corresponding papers indicated in the last column and ordered by MJD.

	Value	Error
t_0 (MJD)	55183.1042	
ν_0 (Hz)	19.7379785	$\pm 1.91 \times 10^{-6}$
$\dot{\nu_0}$ (Hz/s)	-1.86557×10^{-10}	$\pm 9.76 \times 10^{-15}$
$\ddot{\nu_0}$ (Hz/s^2)	3.6638×10^{-21}	$\pm 2.68 \times 10^{-23}$

Table 4.4: The coefficients of the second order polynomial used for the fit.

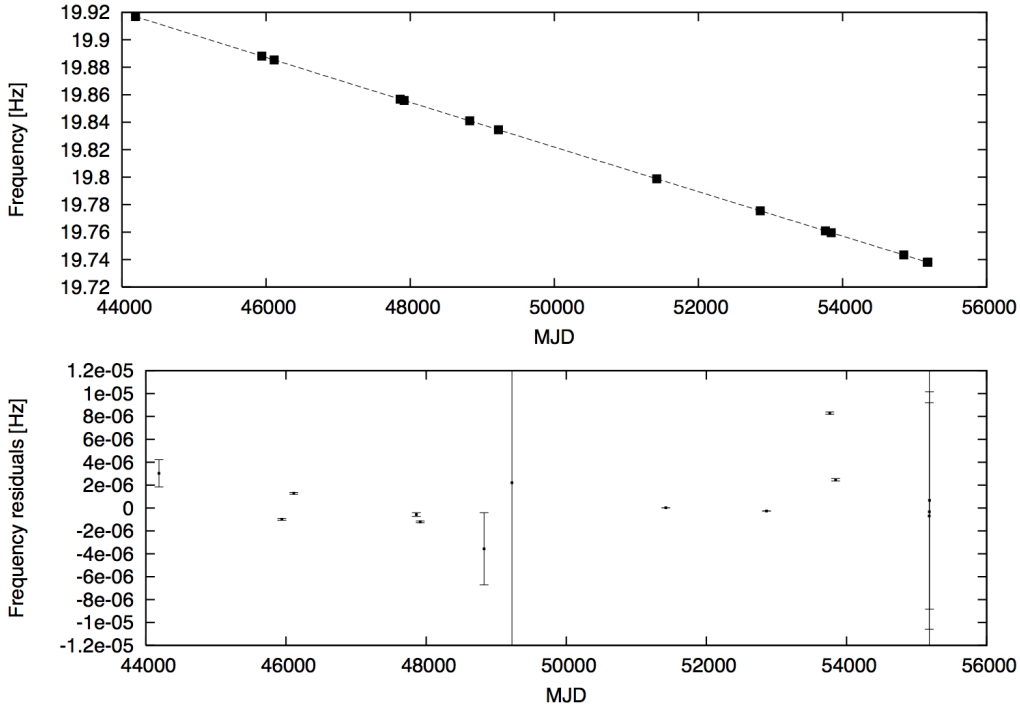

Figure 4.3: Fit over the data shown in Table 4.3.

Our result differs by slightly more than 3 sigmas from the value given by Livingstone by a careful analysis of all X-ray data obtained using 7.6 years of data from the Rossi X-Ray Timing Explorer, and it confirms that the value of the braking index for this pulsar is definitely lower than 3.

4.4 Conclusions

We have observed the Large Magellanic Cloud PSR B0540-69 with Iqueye, a novel extremely high time resolution photometer, obtaining data of unprecedented timing accuracy. The data provide the most detailed optical light curve available so far for this pulsar, extending to 27 years the time spanned by X-ray, optical and radio data and al- lowing a refined determination of the first and second derivatives of the pulsar spin rate. The resulting value of the braking index, n = 2.087, provides increasingly consistent evidence that the braking index of the LMC pulsar B0540-69 is slightly higher than n = 2, and definitely smaller than the magnetic dipole value n = 3, in agreement with the findings for all young pulsars for which it has been possible to perform such measurement (with the possible exception of PSR J1119-6127 for which it has been measured as n = 2.91; Camilo et al. (2000)).

Chapter 5

Multiwavelength emission analysis

Searching for an optical pulsar isn't a simple task. As in the other energy bands, also in optical, the pulses from a pulsar are a series of repeating but faint and noisy light curves: each time the pulsar rotates, its brightness rises and falls producing a light curve, with each curve representing an individual optical pulse. In this context, it is clear that the observation of a new optical pulsar can hardly happens accidentally: it needs first the identification of a possible candidate. Historically, X-ray and γ-ray observations have led to pulsar optical identifications, with all the presently identified pulsars also detected at high energies: 5 out of the 7 γ-ray pulsars detected by NASA's Compton Gamma-Ray Observatory satellite between 1991 and 2000 have also been detected in the optical (Mignani 2011). In particular, γ-ray detections highlight promising candidates for optical observations, since the emission at both energies seems to correlate with the strength of the

magnetic field at the light cylinder (Shearer & Golden 2001). Figure 5.1 shows the relationship between the peak luminosity and the outer magnetic field, Goldreich-Julian current and canonical age. A clear correlation is seen with all these parameters. These results, both in optical and in gamma, are consistent with a model where the two emissions are coming from a similar source location, specifically the last open-field line at some constant fraction of the light cylinder (Shearer & Golden 2001).

In this chapter, a brief multiwavelength analysis is carried out in order to determine which are the parameters to look for in the search of new optical pulsars.

Since rotation-powered pulsars are observable in a very broad wavelength range from radio to high-energy γ-rays, multiwavelength spectra and profiles can give important clues to the acceleration and emission geometry. Although there are some clear patterns of spectral behavior with pulsar age, the observed multiwavelength light curves show a wide variety of characteristics. With the sole exception of the light curve of the Crab pulsar, where its two peaks are in phase from radio to γ-ray energy, for the other pulsars, the radio peak usually leads the one or two gamma peaks in phase and the soft X-ray peaks are broader and overlap the γ-ray peaks (Harding 2007).

From a theoretical point of view, it is believed that the emissions ranging from radio to γ-rays are produced in different regions of the pulsar magnetosphere. To an approximation, the pulsar may be considered as a non-aligned rotating magnet with a very strong surface magnetic field. Just outside the surface of the neutron star, the Lorentz force on a charged particle is very strong and far exceeds the force of gravitational attraction. As a result, the

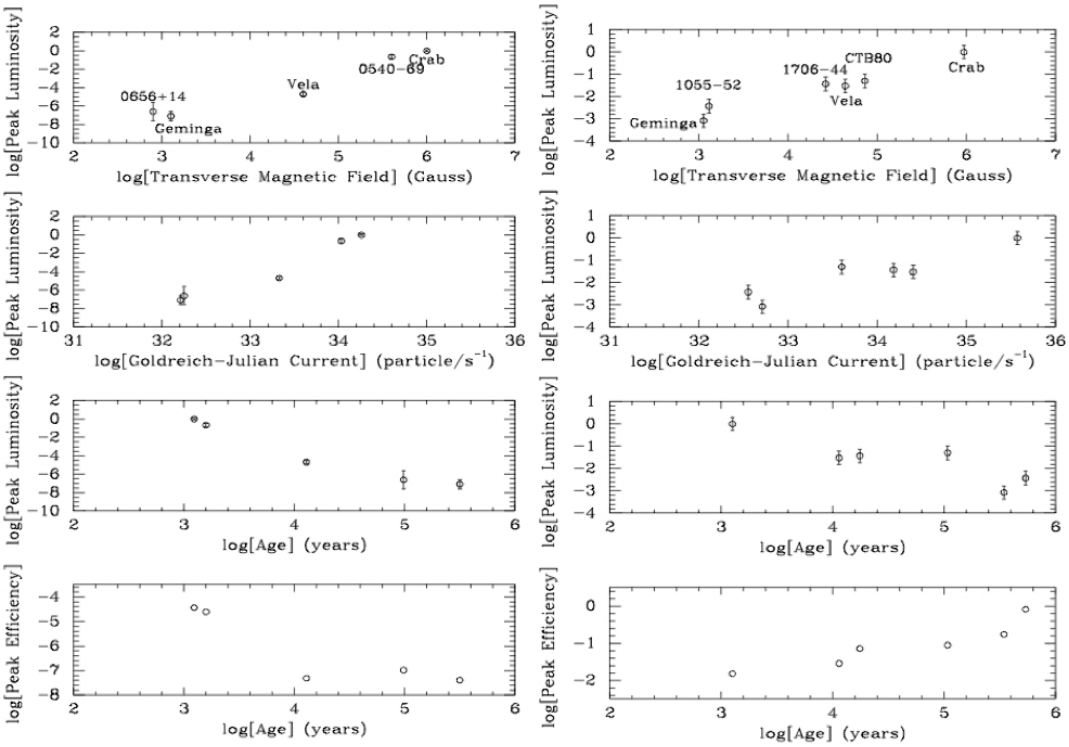

Figure 5.1: Peak optical luminosity (left) and peak gamma-ray luminosity (right) vs. light-cylinder field, Goldreich and Julian current and canonical age. Also shown is the efficiency of the peak emission against age. The peak luminosity has been normalized to the Crab pulsar. The error bars represent both statistical errors from the pulse shape and uncertainty in the pulsar distance (Shearer & Golden 2001).

structure of the magnetosphere of the neutron star is completely dominated by electromagnetic forces. Since the induced electric fields at the surface of a neutron star are very strong, there must be a plasma surrounding the neutron star. In this way, there is a fully conducting plasma surrounding the neutron star and electric currents can flow in the magnetosphere (Longair 2010). If the $E_{||}$ component of the electric field along the magnetic field direction is non-zero in the pulsar magnetosphere it can accelerate particles to ultra-relativistic energies. The accelerated particles emit γ-rays due to various processes, like curvature radiation or synchrotron radiation and inverse Compton scattering (that are produced by the same relativistic electrons but emit radiation at different frequencies). Some of this γ-rays are absorbed giving rise to secondary electron-positron pairs. The created electron-positron pairs screen the electric field $E_{||}$ in the pulsar magnetosphere almost everywhere. The regions where $E_{||}$ is not screened are called accelerators or gaps. These gaps serve as an engine which is responsible for the pulsar non thermal radiation. There are two kind of magnetosphere gaps: polar gaps and outer gaps. The polar gaps place the source of the emission immediately above a magnetic pole. The evidence for the polar gaps came from radio observations of beam width and polarization. The outer gap places the source of emission far out in the magnetosphere, close to the pulsar's light cylinder. The evidence for the origin of the outer gaps came from the high energy radiation observed from young pulsars such as Crab, Vela and Geminga (Cheng et al. 1986).

The radiation of a neutron star has two main components: thermal radiation from the surface of the star and non-thermal (synchrotron) radiation

from its magnetosphere. Synchrotron radiation becomes fainter as the pulsar gets older ($\tau_c > 10^4$ years) and thermal radiation can be detected, starting to show up in the near-UV and then in the X-rays.The synchrotron mechanism of radiation, which can be described by a power law, $F_\nu = F_{\nu_0}(\nu/\nu_0)^{-\alpha}$, prevails at all energy ranges. Tipycally, α, the spectral index, has a value in the range $0 < \alpha < 1$.

If we observe the multiwavelength spectrum of two young pulsars like PSR B0540-69 (Figure 5.2) and Crab (Figure 5.3), we can see that the former has at least two breaks and can be described with several power laws, while the latter shows a smooth transition from X-rays to the optical range. This difference could be due to the fact that the PSR B0540-69 might be heavier, because its progenitor star was a more massive star compared to the Crab progenitor, or it could be that PSR B0540-69 is just more efficient in terms of emitting in the optical and X-rays (Lundqvist 2008).

The Rotating Vector Model

To better understand the emission mechanisms of pulsars, it is important to approach the problem also from a geometrical point of view. Radio astronomers developed the Rotating Vector Model (RVM) to understand the patterns of position angle variation with pulse phase, assuming that radio emitting particles produce radiation polarized either parallel or perpendicular to a dipole magnetic field (Radhakrishnan & Cooke 1969). They showed how the curvature radiation emitted by charged particles will be polarized parallel to the projected direction of the magnetic axis. The position angle of polarization, ψ, measured with respect to the projected direction of the rota-

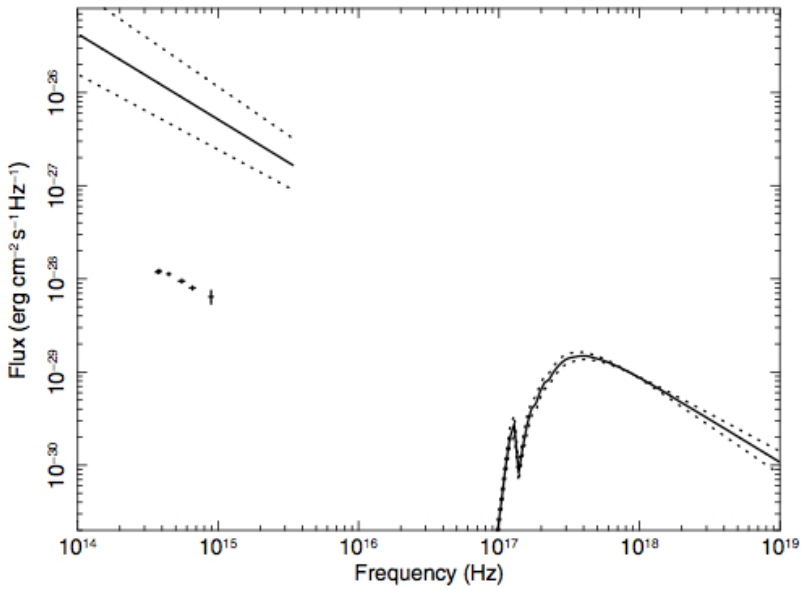

Figure 5.2: Optical spectral energy distribution of PSR B0540-69 (points) compared with the power-law model (Kaaret et al. 2001) best-fitting the Chandra X-ray spectrum (solid line) and its extrapolation in the optical domain (Mignani et al. 2010c).

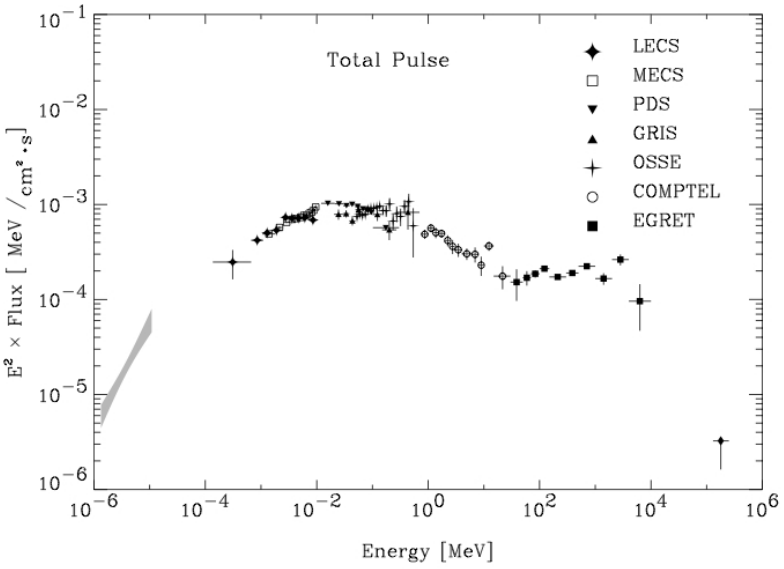

Figure 5.3: The total pulse emission of the Crab pulsar from optical wavelengths up to high-energy gamma-rays. The nebula emission has been subtracted (Kuiper et al. 2001)

tion axis of the pulsar, varies with the pulse phase or longitude ϕ according to the relation

$$\tan\psi = \frac{\sin\alpha \sin\phi}{\sin\zeta\cos\alpha - \cos\zeta\sin\alpha\cos\phi}. \tag{5.1}$$

Here, α is the angle between the rotation and magnetic axes of the pulsar, and ζ that between the rotation axis and our line of sight (Figure 5.4).

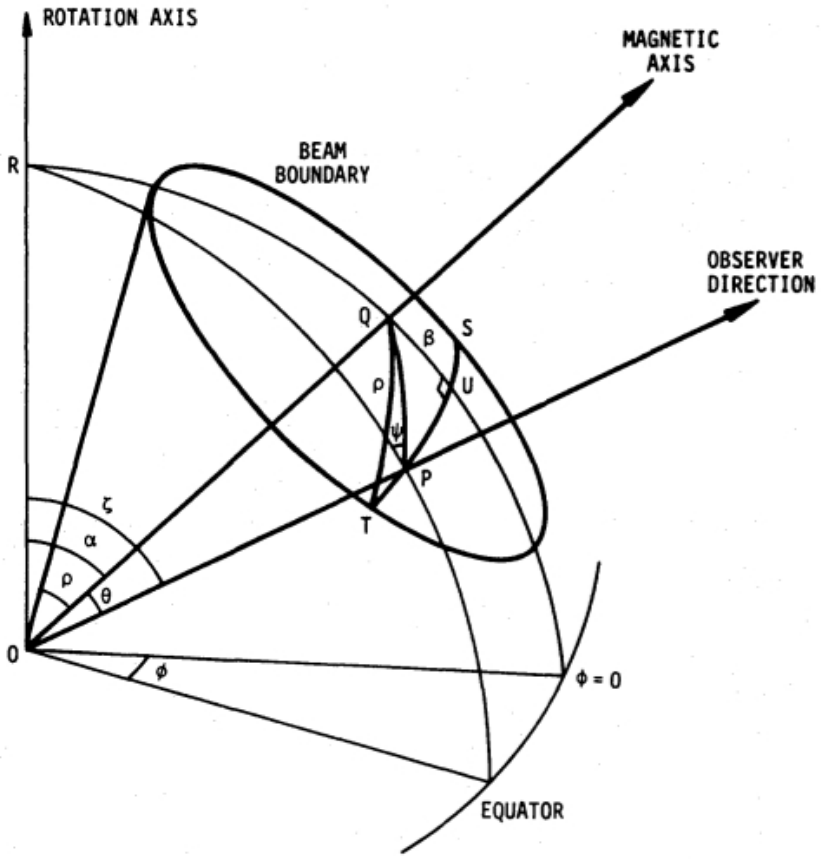

Figure 5.4: Geometry of the polar-cap model for pulsars. We assume that the observer sees radiation from the point P which moves across the arc ST as the star rotates (Lyne & Manchester 1988).

The RVM only works well if the radio emission takes place at altitudes that are a small fraction of the pulsar light cylinder distance. Otherwise, relativistic effects of aberration and retardation will distort the emission pattern. This is precisely why it is not possible to apply this model to the high-energy outer magnetosphere emission models.

High-energy emission models

The models for high-energy pulsar are: polar cap models, where the emission occurs within a few stellar radii of the neutron star surface; slot gap and outer models, where emission occurs in the outer magnetosphere near the light cylinder; and striped wind models, where emission occurs in the pulsar wind outside the light cylinder. The inner and outer magnetosphere emission models give different polarization predictions. Polar cap models assume that particles begin accelerating near the neutron star surface and that γ-rays result from a curvature radiation or inverse Compton induced pair cascade in a strong magnetic field. The slot gap accelerator extends to high altitude along the last open magnetic field line, producing curvature, synchrotron and inverse Compton components in the outer magnetosphere. Outer gap models assume the acceleration occurs in vacuum gaps that form between the null charge surfaces and the light cylinder in the outer magnetosphere and that γ-rays result from curvature radiation and $\gamma - \gamma$ pair production induced cascades. Striped wind models explore the possibility of pulsed emission in the pulsar wind that forms beyond the light cylinder. Thanks to the Fermi satellite (see section 5.2), it is now established that pulsar high-energy emission comes from the outer magnetosphere. As it is deeply explained

in Romani & Watters (2010), the comparison between γ-ray light curves of Fermi LAT pulsars with magnetosphere beaming models allowed greatly improved constraints on the emission zone geometry and the magnetospheric physics: emission starting above the null charge surface (outer gap model) is strongly statistically preferred over models which have substantial emission starting from the stellar surface.

5.1 Optical emission of radio pulsars

The accurate radio positions available for most isolated neutron stars make it easier to determine an optical identification of the object based on the positional coincidence with a putative counterpart, even in relatively crowded regions. Moreover, the knowledge of the pulsar radio ephemeris facilitates the search for pulsations from a candidate optical counterpart.

After the discovery of pulsed optical emission from the radio pulsar PSR 0531+21 in the Crab Nebula, this emission was thought to be synchrotron radiation (Pacini 1971). In 2001, Malov proposed a synchrotron model which can explain the available observations of radio pulsars in hard bands and predict for which sources the probability of detecting hard emission is high. He used a model with an emitting torus localized near the light cylinder: relativistic electrons filling this torus are responsible for the synchrotron luminosity, which can be compared with the observed luminosities of pulsars (Malov 2001). The total synchrotron power of the incoherent electron emission in

the torus L takes the form:

$$L \sim \frac{16\pi^8 e^4 R_\star^6 I}{m^3 c^{11}} \frac{B_0^2 \gamma_b \dot{P} \sin^4\beta \sin^2\psi}{P^8}. \tag{5.2}$$

Here, $R_\star$ is the radius of the neutron star, I is its moment of inertia, $B_0 = B_s \sin\beta$ is the magnetic field at the neutron star surface, β is the angle between the axis of rotation of the neutron star and the magnetic moment $\vec{\mu}$, γ_b is the Lorentz factor in the beam, P is the pulsar period, and $\dot{P}$ is its time derivative. One basic parameter critically affecting the emission is the pitch angle ψ of the emitting charges. The average pitch angle of an emitting electron in the observer's frame is:

$$\bar{\psi} = 1.9 \times 10^3 \frac{\gamma_b P^2}{\gamma_p^2 B_0 \sin^2\beta}. \tag{5.3}$$

The spectrum of synchrotron radiation by relativistic electrons depends substantially on their energy distribution. At $\psi << 1$, the frequency has a maximum at:

$$\nu_m = \frac{0.87\gamma_b^3}{16\sqrt{2\pi} P \gamma_p^2}. \tag{5.4}$$

where γ_p is the Lorentz factor for the electrons of the secondary plasma. Taking the Lorentz factors $\gamma_b = 10^6$ and $\gamma_p = 10$, for five radio pulsars with pulsed optical emission (Shearer et al. 2000) the peak frequencies are in the range from 5.6×10^{14} Hx to 6.6×10^{15} Hz (see Table 5.1).

Since the intensity decreases with decreasing frequency as $\nu^{1/3}$ in the range $\nu < \nu_m$, then, if the emission at the peak is fairly strong, this emission should be detectable at optical frequencies for all the pulsars listed in Table

PSR	P (ms)	$\dot{P}_{-14}$	ν_m (Hz)	log L (erg/s)
B 0531+21	33	42	6.58×10^{15}	28.91
B 0540-69	50	48	4.34×10^{15}	28.24
J 0633+1746	237	11	9.16×10^{14}	23.90
B 0656+14	385	5.5	5.64×10^{14}	23.75
B 0833-45	89	12	2.44×10^{15}	26.64

Table 5.1: Five radio pulsars with pulsed optical emission (Malov 2001).

5.1.

The definitions of L and ψ proposed by the model of Malov (2001) lead to the following proportionality:

$$L \propto \dot{P}/P^4 \tag{5.5}$$

The correlation derived shows that the model can describe the observed optical emission of radio pulsars. From this, Malov predicted that a radio pulsar will produce appreciable optical radiation if $\dot{P}_{-14}/P^4$ is sufficiently large (where $\dot{P}_{-14} = a$ means $\dot{P} = a \times 10^{-14}$). For several objects, the values of this parameter could result in high optical luminosities. If the distance is not extremely large, the pulsars with luminosities $> 10^{28}$ erg/s could be appreciable optical emitters. In Table 5.2 there is a list of such radio pulsars. Optical flux was detected from PSR 1509-58 that has the maximum luminosity among the sources in the list (Becker & Truemper 1997).

The shorter the period of a pulsar, the harder the energy at which the peak of its synchrotron radiation is observed. If the peak frequency in a pulsar spectrum is located at X-ray or even gamma-ray energies, such a pulsar can still emit appreciable optical emission. Among the pulsars listed

PSR	$\dot{P}_{-14}/P^4$	log L (erg/s)	d (kpc)
1046-58	4.06×10^4	28.49	2.98
1338-62	1.82×10^4	28.15	8.66
1509-58	2.96×10^5	29.36	4.40
1610-50	1.76×10^4	28.14	7.26
1706-44	8.59×10^4	28.82	1.82
1727-33	2.28×10^4	28.25	4.24
1757-24	5.24×10^4	28.61	4.61
1800-21	4.22×10^4	28.51	3.94
1823-13	7.08×10^4	28.74	4.12

Table 5.2: Radio pulsars whose luminosity exceeds 10^{28} erg/s (Malov 2001).

by Malov, there are four pulsars that were detected in gamma by the Fermi satellite (see section 5.2): PSR 1046-58, PSR 1509-58, PSR 1706-44 and PSR 1727-33. Except PSR 1509-58 that, as said before, was already been detected in the optical, the other three could then be plausible candidates for future optical observations. It should be noted that there is another radio pulsar analyzed by Malov, PSR 1055-52, which has a luminosity $< 10^{28}$ erg/s but, maybe due to its small distance, $d \sim 1.53$ kpc, was observed both in optical (Mignani et al. 2010) and in gamma.

5.2 High-energy observations with Fermi Telescope

The launch of the Fermi Gamma-Ray Space Telescope (FGST, Figure 5.5), previously called GLAST (Gamma-ray Large Area Space Telescope), on June 11, 2008, from Cape Canaveral (Florida, USA), began a new era in the study of γ-ray pulsars, allowing the detailed study of their spectra and light curves.

The satellite went to low Earth orbit and currently is in a circular orbit, 565 km altitude, with an orbital period of 95 minutes and 25.6° inclination. The satellite scans the entire sky every 192 min (two orbits).

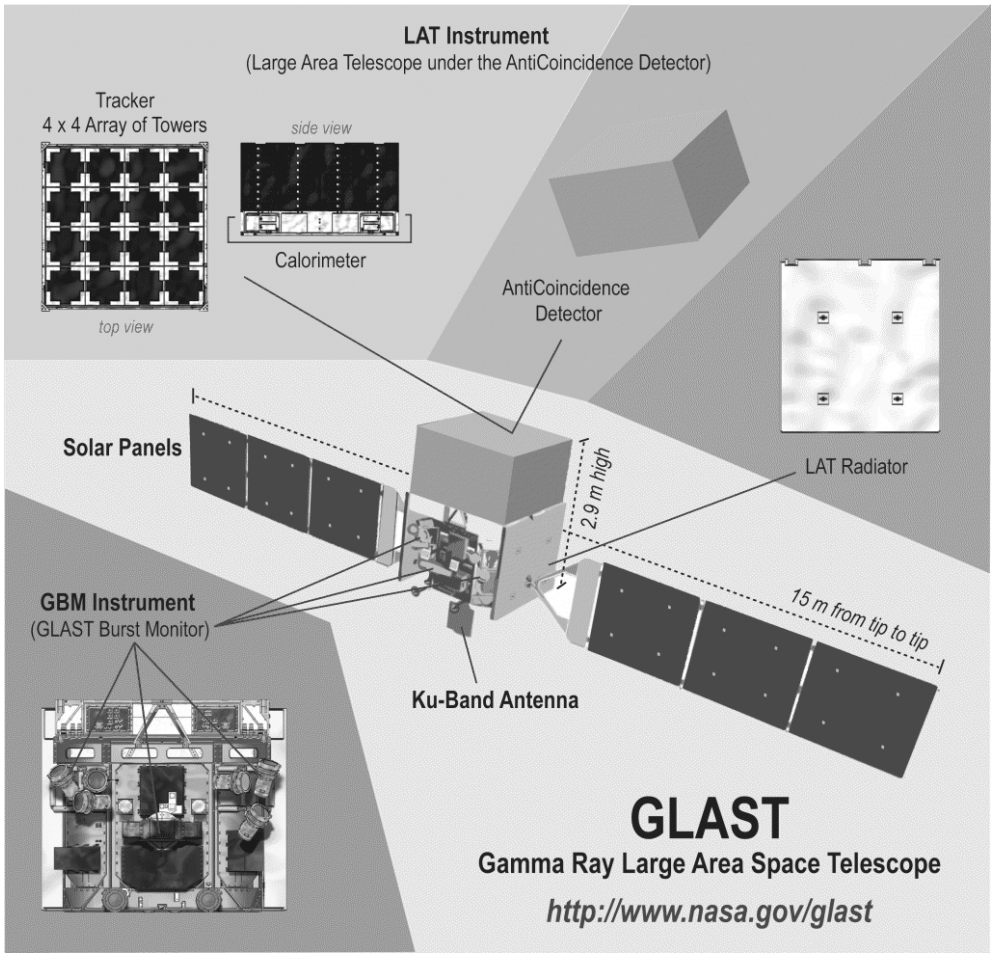

Figure 5.5: A diagram of Fermi with labels for major components (Credit: NASA E/PO, Sonoma State University, Aurore Simonnet).

The telescope has been optimized to measure gamma rays from 20 MeV to 300 GeV, with unprecedented angular resolution in this energy range com-

pared with previous γ-ray missions. It was designed to study γ-ray bursts and background radiation, neutron stars, cosmic rays and supernova remnants, solar flares emitting in γ-rays, and join the search for weakly interacting massive particles.

The main instrument is the Large Area Telescope (LAT, Atwood et al. (2009)). It operates like a particle detector and uses silicon strips to detect high-energy γ-rays with unprecedented resolution and sensitivity. It is a pair-conversion telescope with a precision converter-tracker and calorimeter, each consisting of a 4×4 array of 16 modules. The converter-tracker is made of high-Z material in which γ-rays incident on the LAT can convert to an e^+e^- pair (see Figure 5.6), while the detectors record the passage of charged particles, measuring their tracks. This last information is used to reconstruct the directions of the incident γ-rays. The calorimeter has two primary purposes: to measure the energy deposition due to the electromagnetic particle shower and to image the shower development profile. This last capability enable the high-energy reach of the LAT and contribute significantly to background rejection.

A segmented anti coincident detector covers the tracker array, providing charged-particle background rejection, while a data acquisition system collects the data from the other subsystems, implements the multilevel event trigger, provides onboard event processing to reduce the number of downlinked events and provides also an onboard science analysis platform to rapidly search for transients.

The LAT provides an improvement both in sensitivity and positional accuracy with respect to its predecessors. This translates into a more accurate

Parameter	Value
Energy range	20 MeV - 300 GeV
Effective area at normal incidence	9.500 cm^2
Energy resolution:	
100 MeV - 1 GeV	9%-15%
1 GeV - 10 GeV	8%-9%
10 GeV - 300 GeV	8.5%-18%
Fielf of view	2.4 sr
Timing accuracy	<10 μs
Dead time	26.5 μs

Table 5.3: Summary of LAT instrument parameters and estimated performance (Atwood et al. 2009).

source localization and a much better photon statistics, which facilitates the periodicity search even without a reference radio period and increases the chances to discover new γ-ray pulsars (see Table 5.3 for a summary of its performance).

5.2.1 Optical candidates in the Fermi pulsar catalog

Finding a way to determine possible candidates for optical observations in the Fermi catalog is challenging. Starting from the characteristics of the already known optical pulsars, it is not possible to determine real common features. A clear trend is not visible and pulsars can be assembled in different groups, depending on the chosen parameters. It could be, for example, the distance, since it usually greatly influences optical observations. Even for this parameter, however, two optical pulsars like Crab and PSR B0540-69, so similar for other reasons, differ extremely: the former is located at ~ 2 kpc, the latter at ~ 49 kpc.

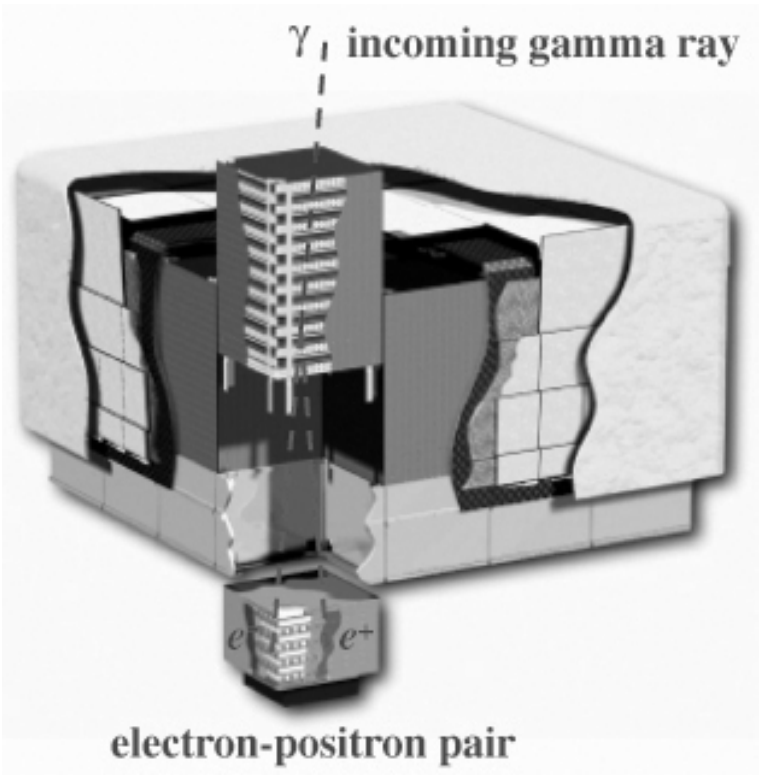

Figure 5.6: Cutaway of the LAT instrument showing an inside view of one of the towers as an incoming gamma ray interacts producing an electron-positron pair (Credit: LAT Collaboration).

The only starting point, then, is to find a way to maximize the detection probability. In this context, radio observations play an important role since they provide measurements of the pulsar distance and of the pulsar rotational energy loss. Assuming that there is a conversion factor between the rotational energy loss and the optical luminosity, it is then possible to estimate the expected optical brightness of the pulsar. But high-energy observations are also extremely important since, for example, X-ray observations can provide an estimate of the distance of pulsars which are radio-silent. Moreover, if we assume that the luminosity scale in a similar way from X-ray and γ-ray to optical, the analysis of their spectrum provides expected values for the pulsar optical brightness. In case of no break in the pulsar magnetospheric emission (as in the case of the Crab pulsar, see Figure 5.3), it could be even possible to determine the optical spectrum.

So, in order to maximize the detection probability, Mignani et al. suggested the following characteristics for a first selection: a pulsar rotational energy loss $\dot{E} > 10^{34}$ erg/s, a spin-down age $\tau < 1$ Myr, to sample the younger and more energetic LAT pulsar population, a γ-ray flux $F_\gamma > 10^{-10}$ erg/cm^2/s (at 100 MeV), a distance lower than ~ 2.5 kpc and an hydrogen column density N_H not larger than $\sim 10^{21}$ cm^{-2}, not to be limited by the interstellar extinction. Figure 5.7 highlights the region (grey area) in the $P - \dot{P}$ diagram in which $\dot{E} > 10^{34}$ erg/s and $\tau < 1$ Myr.

Based on these two last parameters and on the distance, a first selection of pulsars is shown in the Table 5.4. Some of these are already known optical pulsars: PSR J0534+2200, PSR J0633+1746, PSR J0659+1414 and PSR J0835-4510. Among the others, one of the most interesting target is

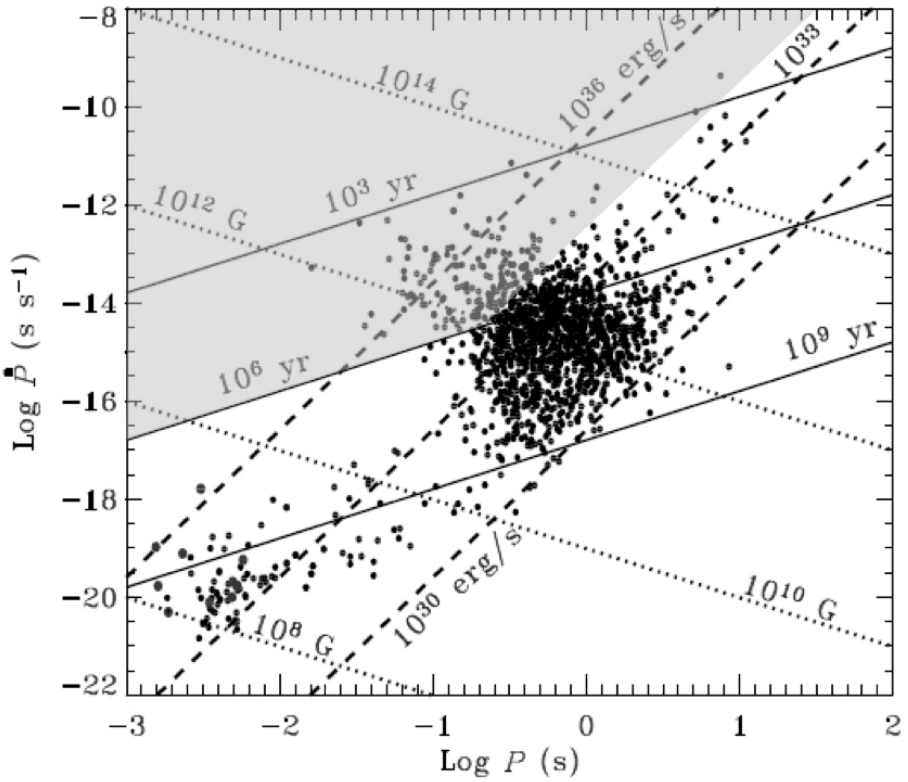

Figure 5.7: The grey area highlights the zone in the $P - \dot{P}$ diagram in which $\dot{E} > 10^{34}$ erg/s and $\tau < 1$ Myr.

PSR J1709-4429 (or PSR B1706-44) since this is also one of the radio pulsar identified as possible optical candidate.

Pulsar	d (kpc)	τ (Myr)	$\dot{E}$ (10^{34} erg/s)
J0007+7303	1.4	0.014	45.2
J0248+6021	2	0.063	21
J0534+2200	2	0.001	46100
J0633+1746	0.16	0.34	3.3
J0659+1414	0.29	0.11	3.8
J0742-2822	2.07	0.16	14.3
J0835-4510	0.294	0.011	688
J1028-5819	2.3	0.09	83.2
J1057-5226	1.38	0.54	3
J1709-4429	1.82	0.018	341
J1747-2958	2.01	0.026	251
J1809-2332	1.8	0.068	43
J1952+3252	2.5	0.11	374

Table 5.4: Selection of Fermi pulsars based on the values of distance, age and rotational energy loss.

5.3 An optical candidate: PSR B1706-44

Both the analysis performed on radio pulsars and on high-energy pulsars brought to the conclusion that PSR B1706-44 (or PSR J1709-4429) could be a possible candidate for optical observations.

PSR B1706-44 is a young pulsar with a period of about 102 ms. It was discovered during a radio survey of the southern hemisphere (Johnston et al. 1992) and has been identified as a γ-ray pulsar by the EGRET instrument aboard the Compton Gamma Ray Observatory by using the radio timing information (Thompson et al. 1999).

Pulsar	P (ms)	$\dot{P}$ (10^{-15})	$\dot{E}$ 10^{34} erg s^{-1}	Age (10^3 G)	$B_{surface}$ (10^{12} G)	Distance (kpc)
PSR B1706-44	102	93	341	17.5	3.12	1.4 - 3.6

Table 5.5: Various characteristic parameters for the PSR B1706-44 (Abdo et al. 2010).

PSR B1706-44 was observed by the Fermi LAT and an analysis of data collected in a period of 13 months, from 2008 August 4 (MJD 54682.66) to 2009 August 28 (MJD 55071.94), is described in Abdo et al. (2010). Figure 5.8 shows the pulse profiles in separate energy bands for two rotation cycles. The full energy band pulse profile (top panel) clearly shows a two peaks structure. A third peak is seen above 3 GeV, similar to what is observed in the Vela pulsar.

PSR B1706-44 has many characteristics in common with the Vela pulsar: their spin periods as well as the age and the rotational energy loss. Furthermore, their multiwavelength behavior is comparable, with a similar spin-down power conversion efficiency both in soft X-rays and high-energy γ-rays. Assuming that these similarities hold also in the optical domain and scaling the magnitude of Vela (V=23.6, d=500 pc) for the distance of PSR 1706-44 ($\sim$1.8 kpc), Mignani et al. (1999) get a rough magnitude of $V \sim 26$, to which a correction of at least one magnitude must be added to account for the higher interstellar absorption. In the same paper, a deep optical observation for this pulsar was performed, determining a limiting magnitude of $V \sim 27.5$. However, no optical counterpart was detected. These results set also an upper limit on its optical luminosity, varying from $\sim 2 \times 10^{28}$ to $\sim 5 \times 10^{29}$ erg/s, depending on the exact amount of interstellar absorption.

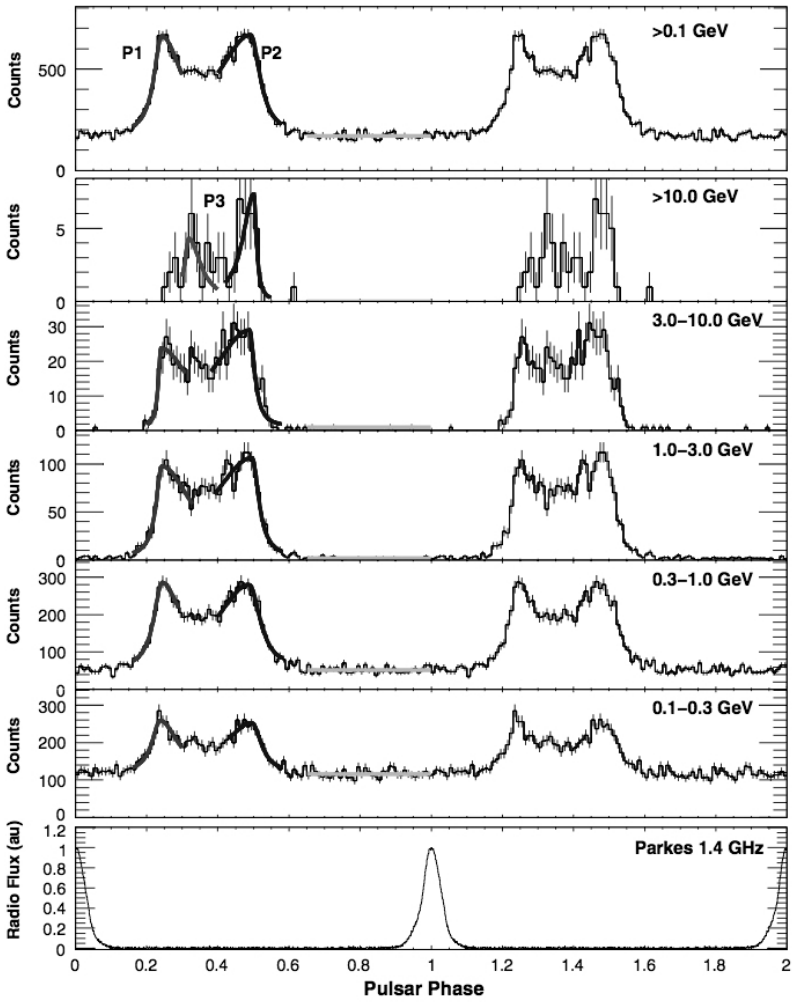

Figure 5.8: Energy dependence of the PSR B1706-44 pulse profile The top panel is the pulse profile in the full energy band. The following five panels show the pulse profile in five different energy bands (Abdo et al. 2010). The bottom panel shows the pulse profile at radio wavelengths at 1.4 GHz provided by the Parkes radio telescope.

Since we are dealing with a probably very faint source, right now only new observations with telescope like the Very Large Telescope (VLT), a telescope operated by the ESO in Cerro Paranal (Chile), could give higher chances for an optical detection of the pulsar. And in this context, the use of a photometer like Iqueye, adapted for the VLT, could only enhance the possibilities of new discoveries.

Conclusions

Aqueye and Iqueye are two fixed-aperture photometers which collect the light within a field of view of few arcseconds around the target object. The first was built to be mounted at the Asiago telescope (Italy), the latter at the ESO New Technology Telescope in La Silla (Chile). They represents the first attempts to overcome the difficulties in the observation of optical pulsars by using instruments capable of properly analyze the timing signature of rapidly varying sources.

From the theoretical point of view, Iqueye was analyzed in order to evaluate its performance when dealing with optical pulsars. The expected number of photons from the sky in La Silla and from the three pulsars were calculated and adapted to the efficiency of the instrument. Then, as proof, a comparison was done with the real detected number of photons of PSR B0540-69 obtained during the night of December 18, 2009, the one with the best S/N ratio. The result confirms the good quality of the observation and also set a method to evaluate future similar observations.

As a further prove of the quality of these instruments, we reported also the results obtained by Aqueye observing the Crab pulsar in 2008. These observations allowed the determination of the optical light curve of this pulsar

and a comparison between the phase of the Crab pulsar with that reported in the radio archive at the Jodrell Bank Observatory.

The central part of the thesis focuses on the analysis of the data obtained by Iqueye in January and December 2009 observing PSR B0540-69. This is the second brightest pulsar in the optical band, located in the Large Magellanic Cloud. The determination of its period led to the publication of its optical light curve: the first one in more than ten years. Combining our frequency values to the previously published data sets, we calculated the first and second frequency derivatives. Fitting these values with a second order polynomial, we determined not only the first derivative of the frequency but also the second derivative. With the so determined values of the frequency, we were able to calculate the value of the braking index, a parameter which provides insight into the physics of the pulsar mechanism, confirming that for this pulsar it is definitely lower than 3.

The last part of this work explores the multiwavelength emission of pulsars. The idea was to identify possible candidates for optical observations starting from the known radio and gamma pulsars. Using a previously developed emission model for radio pulsars, a group of interesting candidates for optical observations was found. Then this group of pulsars was interpolated with the γ-ray pulsar catalog of Fermi LAT, the main instrument of the Fermi Gamma-ray Space Telescope. In this way, we were able to isolate a possible candidate for optical observations, PSR 1706-44. This pulsar was already observed in the optical without success but the considerations made in this thesis encourage the planning of new attempts with telescope like the Very Large Telescope at the ESO facilities in Cerro Paranal (Chile) and

optimized instrument like Iqueye.

From this last perspective, a project has been already proposed to build the Twin Advanced Iqueye (TAI), that consists of a couple of extremely high sensitivity and high time resolution photon counting photometers to be applied at the VLTs. TAI will be able to time tag up to 80 million events per second with an absolute time accuracy better than 50 ps over hours of continuous observations, improving by orders of magnitudes the performance of the presently available common astronomical fast photometers. This will allow to begin the investigation of unexplored time domains. The reason for building two identical units is, in fact, to largely improve the scientific return of this type of instrumentation: using simultaneously two units on two VLTs, we will realize, for the first time, post processing photon correlation measurements from astronomical objects, opening the way to quantum astronomy observations.

Summary of original contributions

Part of the work reported in this thesis was done with Iqueye, a high speed photometer built for the 3.6 m New Technology Telescope of ESO in La Silla (Chile), both from a theoretical and an experimental way.

- The theoretical aspect was approached from the point of view of the performance of the instrument when dealing with astrophysical objects like optical pulsars. The procedure conceived and adopted is described in section 3.2. The idea was to calculate the theoretical number of photons expected when observing the three main optical pulsars (Crab, B0540-69 and Vela) and then compare the results with real data. In doing that, it was also necessary to calculate the spectrum of the sky in La Silla and combine it with the efficiency spectrum of Iqueye. The procedure adopted demonstrated the good quality of our data and also resulted to be a practical way to test the quality of future observations.

- From an experimental point of view, Iqueye was tested during the nights of observation carried out in 2009. Chapter 4 fully describes the observations of PSR B0540-69. The analysis of the collected data led to the publication of an original paper: Gradari et al. (2011). The

most important result of this work was the publication of the optical light curve of this pulsar: it was the first published since 1996. Given the high number of photons and the extremely accurate time tagging guaranteed by Iqueye, we feel also confident to say that this light curve (Figure 4.2) is also the best available so far in visible light. With our data alone, obtained over a time span of one year, we were able to determine the first derivative of the frequency, founding a value in good agreement with those available in the literature. Adding our values to previously published data sets, it was then possible to determine also the second frequency derivative. With the so determined values of time, frequency and frequency derivatives, we were able to calculate the braking index, a parameter that provides insight into the physics of the pulsar mechanism, and the characteristic age of the pulsar.

A third important analysis that has been done in this thesis is described in Chapter 5.

- A multiwavelength emission analysis was carried out in order to find new possible pulsar condidates for future optical observations. Starting from pulsar emission models found in the literature, some possible candidates were found both in radio and in gamma. The idea developed in this chapter was to correlate the results found at the two extreme of the spectrum. This led to the isolation of a pulsar as the most interesting candidate: PSR B1706-44 (Section 5.3). Even if, until now, optical observations of this pulsar led to no results, the theoretical outcomes of this thesis encourage further surveys, possibly with bigger telescopes

and optimized instruments.

Ringraziamenti

Grazie al Prof. Cesare Barbieri e al Prof. Giampiero Naletto per avermi seguito nel corso di questi tre anni di dottorato. La disponibilità e la comprensione che avete dimostrato nei miei confronti mi hanno permesso di crescere e maturare non solo a livello scientifico.

Grazie a Francesco Longo per essere stato al mio fianco anche in questa avventura padovana, per il tempo che mi hai dedicato, per i consigli e per l'amicizia che non manchi mai di dimostrarmi.

Un ringraziamento speciale va a David Smith e al gruppo Fermi di Bordeaux per avermi accolto, aiutato e guidato con una tale gentilezza, allegria e pazienza che mi portano a ripensare a quei mesi francesi come una delle più belle esperienze che mi siano finora capitate.

In questi anni ho avuto la possibilità di conoscere e frequentare diverse persone che, oltre a essere sempre disponibili per consigli e aiuti, non mi hanno mai fatto mancare un sorriso o il piacere di una chiacchierata. In particolare voglio ringraziare Elettra, Francesca, Paolo e Leonardo, la cui amicizia conto di portare via con me ben oltre questa esperienza.

Grazie a Ivano per essere stato il miglior compagno di ufficio che potessi immaginare. Temo che dovrai sopportarmi ancora a lungo perché la tua

ironia, la tua comprensione e la tua amicizia sono stati talmente importanti per me che conto di usufruirne ancora per molto tempo.

Grazie a Anastasia, Margherita, Elisa e Matteo. Pur essendo lontani dalle dinamiche del mio mondo scientifico, siete sempre al mio fianco per ascoltarmi, sostenermi e farmi ridere come pochi. Sono orgogliosa di chiamarvi amici.

Infine, un pensiero importante va alla mia famiglia. Grazie a nonna Gioia per il sostegno e l'amore incondizionato. Grazie a mamma e papà per essere, come sempre, al mio fianco con parole, abbracci e baci che mi rendono più forte. Grazie a Simona per essere una sorella più dolce, forte e divertente di quanto mi meriti.

List of Figures

List of Tables

Bibliography

Abdo, A. A., Ackermann, M., Ajello, M., et al. 2010, The Astrophysical Journal Supplement, 187, 460

Abdo, A. A., Ajello, M., Antolini, E., et al. 2010, Astrophysical Journal, 720, 26

Allen, M. P. & Horvath, J. E. 1997, Astrophysical Journal v.488, 488, 409

Anderson, P. W. & Itoh, N. 1975, Nature, 256, 25

Arecchi, F. T., Courtens, E., Gilmore, R., & Thomas, H. 1972, Physical Review A, 6, 2211

Atwood, W. B., Abdo, A. A., Ackermann, M., et al. 2009, The Astrophysical Journal, 697, 1071

Barbieri, C. 2007, Memorie della Società Astronomica Italiana Supplement, 11, 74

Barbieri, C., Naletto, G., Capraro, I., et al. 2010, Advanced Photon Counting Techniques IV. Edited by Itzler, 7681, 24

Barbieri, C., Naletto, G., Occhipinti, T., et al. 2007, Memorie della Società Astronomica Italiana Supplement, 11, 190

Barbieri, C., Naletto, G., Verroi, E., et al. 2009, Science with the VLT in the ELT Era, 249

Becker, W. & Truemper, J. 1997, Astronomy and Astrophysics, 326, 682

Boyd, P. T., van Citters, G. W., Dolan, J. F., et al. 1995, Astrophysical Journal, 448, 365

Camilo, F., Kaspi, V. M., Lyne, A. G., et al. 2000, Astrophysical Journal, 541, 367

Campana, R., Mineo, T., de Rosa, A., et al. 2008, Monthly Notices of the Royal Astronomical Society, 389, 691

Capraro, I., Barbieri, C., Naletto, G., et al. 2010, Quantum Information and Computation VIII. Edited by Donkor, 7702, 18

Capraro, I., Naletto, G., Barbieri, C., et al. 2009, Proceedings of the Quantum of Quasars workshop. December 2-4, 12

Carramiñana, A., Vidrih, S., & Cadez, A. 2005, II International GTC Workshop: Science with GTC 1st-light Instruments and the LMT (Eds. A. M. Hidalgo-Gámez), 24, 61

Chakrabarty, D. & Kaspi, V. M. 1998, Astrophysical Journal Letters v.498, 498, L37

Chanan, G. A., Helfand, D. J., & Reynolds, S. P. 1984, Astrophysical Journal, 287, L23

Cheng, K., Ruderman, M., & Zhang, L. 2000a, Highly Energetic Physical Processes and Mechanisms for Emission from Astrophysical Plasmas, 195, 223

Cheng, K. S., Ho, C., & Ruderman, M. 1986, Astrophysical Journal, 300, 500

Cheng, K. S., Ruderman, M., & Zhang, L. 2000b, The Astrophysical Journal, 537, 964

Cusumano, G., Massaro, E., & Mineo, T. 2003, Astronomy and Astrophysics, 402, 647

de Luca, A., Mignani, R. P., Caraveo, P. A., & Bignami, G. F. 2007, The Astrophysical Journal, 667, L77

Deeter, J. E., Nagase, F., & Boynton, P. E. 1999, Astrophysical Journal, 512, 300

Dickel, J. R., Mulligan, M. C., Klinger, R. J., et al. 2002, Neutron Stars in Supernova Remnants, 271, 195

Dravins, D., Barbieri, C., Fosbury, R. A. E., et al. 2005a, IAU, 1, 502

Dravins, D., Barbieri, C., Fosbury, R. A. E., et al. 2005b, eprint arXiv, 11027

Edwards, R. T., Hobbs, G. B., & Manchester, R. N. 2006, Monthly Notices of the Royal Astronomical Society, 372, 1549

Elsworth, Y. P. & James, J. F. 1981, Astronomy and Astrophysics, 103, 131

Germaná, C., Zampieri, L., Barbieri, C., et al. 2011, Astronomy and Astrophysics

Germanà, C., Zampieri, L., Capraro, I., et al. 2008, Proceedings of "Polarimetry days in Rome: Crab status, 31

Ghosh, P. 2007, Rotation and Accretion Powered Pulsars, World Scientific Series in Astronomy and Astrophysics (Singapore: World Scientific)

Glauber, R. J. 1963a, Physical Review Letters, 10, 84

Glauber, R. J. 1963b, Physical Review, 130, 2529

Glauber, R. J. 1963c, Journal of Mathematical Physics, 4, 294

Gold, T. 1968, Nature, 218, 731

Goldreich, P. & Julian, W. H. 1969, Astrophysical Journal, 157, 869

Gotthelf, E. V., Zhang, W., Marshall, F. E., Middleditch, J., & Wang, Q. D. 2002, Neutron Stars in Supernova Remnants, 271, 365

Gouiffes, C., Finley, J. P., & Oegelman, H. 1992, Astrophysical Journal, 394, 581

Gradari, S., Barbieri, M., Barbieri, C., et al. 2011, Monthly Notices of the Royal Astronomical Society, 412, 2689

Gregory, P. C. & Loredo, T. J. 1992, Astrophysical Journal, 398, 146

Haensel, P., Potekhin, A., & Yakovlev, D. 2007, Neutron Stars I (Springer)

Hanbury Brown, R. 1974, The intensity interferometer. Its applications to astronomy (Hanbury Brown, R.)

Harding, A. K. 2007, eprint arXiv, 0710, 3517

Hewish, A., Bell, S. J., Pilkington, J. D. H., Scott, P. F., & Collins, R. A. 1968, Nature, 217, 709

Hill, R. J., Dolan, J. F., Bless, R. C., et al. 1997, Astrophysical Journal Letters v.486, 486, L99

Hobbs, G., Lyne, A. G., Kramer, M., Martin, C. E., & Jordan, C. 2004, Monthly Notices of the Royal Astronomical Society, 353, 1311

Hobbs, G. B., Edwards, R. T., & Manchester, R. N. 2006, Monthly Notices of the Royal Astronomical Society, 369, 655

Janssen, G. H. & Stappers, B. W. 2007, Proceedings of the 363. WE-Heraeus Seminar on Neutron Stars and Pulsars 40 years after the discovery., 80

Johnston, S., Lyne, A. G., Manchester, R. N., et al. 1992, Monthly Notices of the Royal Astronomical Societ, 255, 401

Johnston, S., Romani, R. W., Marshall, F. E., & Zhang, W. 2004, Monthly Notices of the Royal Astronomical Society, 355, 31

Kaaret, P., Marshall, H. L., Aldcroft, T. L., et al. 2001, The Astrophysical Journal, 546, 1159

Kramer, M., Lyne, A. G., Hobbs, G., et al. 2003, The Astrophysical Journal, 593, L31

Kramer, M., Xilouris, K. M., Jessner, A., et al. 1997, Astronomy and Astrophysics, 322, 846

Kuiper, L., Hermsen, W., Cusumano, G., et al. 2001, Astronomy and Astrophysics, 378, 918

Large, M. I., Vaughan, A. E., & Mills, B. Y. 1968, Nature, 220, 340

Larsson, S. 1996, Astronomy and Astrophysics Supplement, 117, 197

Lattimer, J. M. & Prakash, M. 2001, The Astrophysical Journal, 550, 426

Lattimer, J. M. & Prakash, M. 2004, Science, 304, 536

Lattimer, J. M. & Prakash, M. 2007, Physics Reports, 442, 109

Leahy, D. A. 1987, Astronomy and Astrophysics, 180, 275

Leahy, D. A., Elsner, R. F., & Weisskopf, M. C. 1983, Astrophysical Journal, 272, 256

Livingstone, M. A., Kaspi, V. M., & Gavriil, F. P. 2005, The Astrophysical Journal, 633, 1095

Livingstone, M. A., Kaspi, V. M., Gavriil, F. P., et al. 2007, Astrophysics and Space Science, 308, 317

Longair, M. S. 2010, High Energy Astrophysics (Cambridge University Press), 369

Lorimer, D. R. & Kramer, M. 2005, Handbook of Pulsar Astronomy (Cambridge University Press)

Lundqvist, N. 2008, The young pulsar B0540-69.3 and its surroundings (Stockholm University 2008)

Lyne, A. G. & Manchester, R. N. 1988, Monthly Notices of the Royal Astronomical Society, 234, 477

Lyne, A. G., Pritchard, R. S., & Graham-Smith, F. 1993, Monthly Notices of the Royal Astronomical Society, 265, 1003

Machabeli, G. & Osmanov, Z. 2009, The Astrophysical Journal Letters, 700, L114

Malov, I. F. 2001, Astronomy Reports, 45, 865

Malov, I. F. & Machabeli, G. Z. 2001, The Astrophysical Journal, 554, 587

Manchester, R. N., Hobbs, G. B., Teoh, A., & Hobbs, M. 2005, The Astronomical Journal, 129, 1993

Manchester, R. N., Mar, D. P., Lyne, A. G., Kaspi, V. M., & Johnston, S. 1993a, Astrophysical Journal, 403, L29

Manchester, R. N. & Peterson, B. A. 1989, Astrophysical Journal, 342, L23

Manchester, R. N., Staveley-Smith, L., & Kesteven, M. J. 1993b, Astrophysical Journal, 411, 756

Manchester, R. N. & Taylor, J. H. 1977, Pulsars / Richard N. Manchester, Joseph H. Taylor (W. H. Freeman, San Francisco), 281

Massaro, E., Campana, R., Cusumano, G., & Mineo, T. 2006, Astronomy and Astrophysics, 459, 859

Middleditch, J. & Kristian, J. 1984, Astrophysical Journal, 279, 157

Middleditch, J. & Pennypacker, C. 1985, Nature, 313, 659

Middleditch, J., Pennypacker, C. R., & Burns, M. S. 1987, Astrophysical Journal, 315, 142

Mignani, R., Caraveo, P. A., & Bignami, G. F. 1997, Astrophysical Journal Letters v.474, 474, L51

Mignani, R. P. 2007, eprint arXiv, 0710, 5374

Mignani, R. P. 2009, eprint arXiv, 0908, 1010

Mignani, R. P. 2010, eprint arXiv, 1008, 5037

Mignani, R. P. 2011, Advances in Space Research, 47, 1281

Mignani, R. P., Caraveo, P. A., & Bignami, G. F. 1999, Astronomy and Astrophysics, 343, L5

Mignani, R. P., Jackson, A. C., & Spiers, A. 2010, Astronomy and Astrophysics, 520, A21

Mignani, R. P., Jackson, A. C., & Spiers, A. 2010a, Astronomy and Astrophysics, 520, 21

Mignani, R. P., Mereghetti, S., Gouiffes, C., & Caraveo, P. A. 1998, The Messenger, 94, 25

Mignani, R. P., Pavlov, G. G., de Luca, A., & Caraveo, P. A. 2004, Advances in Space Research, 33, 518

Mignani, R. P., Pavlov, G. G., & Kargaltsev, O. 2010b, The Astrophysical Journal, 720, 1635

Mignani, R. P., Sartori, A., de Luca, A., et al. 2010c, Astronomy and Astrophysics, 515, 110

Mignani, R. P., Shearer, A., de Luca, A., et al. 2011, Astronomy & Astrophysics, 533, 101

Mignani, R. P., Zharikov, S., & Caraveo, P. A. 2007, Astronomy and Astrophysics, 473, 891

Mineo, T., Cusumano, G., Massaro, E., et al. 1999a, Astronomy and Astrophysics, 348, 519

Mineo, T., Cusumano, G., Segreto, A., et al. 1999b, Nuclear Physics B Proceedings Supplements, 69, 257

Naletto, G., Barbieri, C., Occhipinti, T., et al. 2009, Astronomy and Astrophysics, 508, 531

Naletto, G., Barbieri, C., Verroi, E., et al. 2010, Ground-based and Airborne Instrumentation for Astronomy III. (Edited by McLean), 7735, 138

O'Connor, P., Golden, A., & Shearer, A. 2005, The Astrophysical Journal, 631, 471

Oosterbroek, T., Cognard, I., Golden, A., et al. 2008, Astronomy and Astrophysics, 488, 271

Oppenheimer, J. R. & Volkoff, G. M. 1939, Physical Review, 55, 374

Pacini, F. 1967, Nature, 216, 567

Pacini, F. 1971, Astrophysical Journal, 163, L17

Pacini, F. & Salvati, M. 1983, Astrophysical Journal, 274, 369

Page, D. & Reddy, S. 2006, Annual Review of Nuclear and Particle Science, 56, 327

Pavlov, G. G., Welty, A. D., & Cordova, F. A. 1997, Astrophysical Journal Letters, 489, L75

Petre, R., Hwang, U., Holt, S. S., & Williams, R. M. 2004, Young Neutron Stars and Their Environments, 218, 189

Petrova, S. A. 2003, Monthly Notice of the Royal Astronomical Society, 340, 1229

Petrova, S. A. 2009, The Low-Frequency Radio Universe ASP Conference Series, 407, 309

Plaa, J. D., Kuiper, L., & Hermsen, W. 2003, Astronomy and Astrophysics, 400, 1013

Radhakrishnan, V. & Cooke, D. J. 1969, Astrophysics Letters, 3, 225

Ransom, S. M., Eikenberry, S. S., & Middleditch, J. 2002, The Astronomical Journal, 124, 1788

Richichi, A., Barbieri, C., Fors, O., & Naletto, G. 2009, The Messenger, 135, 32

Romani, R. W. 1996, Astrophysical Journal v.470, 470, 469

Romani, R. W. & Watters, K. P. 2010, The Astrophysical Journal, 714, 810

Serafimovich, N. I., Lundqvist, P., Shibanov, Y. A., & Sollerman, J. 2005, Advances in Space Research, 35, 1106

Serafimovich, N. I., Shibanov, Y. A., Lundqvist, P., & Sollerman, J. 2004, Astronomy and Astrophysics, 425, 1041

Seward, F. D. & Harnden, F. R. 1994, Astrophysical Journal, 421, 581

Seward, F. D., Harnden, F. R., & Helfand, D. J. 1984, Astrophysical Journal, 287, L19

Shearer, A. 2008, High Time Resolution Astrophysics, 351, 1

Shearer, A. & Golden, A. 2001, The Astrophysical Journal, 547, 967

Shearer, A. & Golden, A. 2002, Proceedings of the 270. WE-Heraeus Seminar on Neutron Stars, 44

Shearer, A., Golden, A., & Beskin, G. 2000, Pulsar Astronomy - 2000 and Beyond, 202, 307

Shearer, A., Golden, A., Harfst, S., et al. 1998, Astronomy and Astrophysics, 335, L21

Shearer, A., Golden, A., O'Conner, P., Beskin, G., & Redfern, M. 1999, Irish Astronomical Journal, 26, 99

Shearer, A., Redfern, M., Pedersen, H., et al. 1994, Astrophysical Journal, 423, L51

Shearer, A., Redfern, R. M., Gorman, G., et al. 1997, Astrophysical Journal Letters v.487, 487, L181

Shearer, A., Stappers, B.and O'Connor, P., & al. 2003, Science, 301

Shibanov, Y. A., Zharikov, S. V., Komarova, V. N., et al. 2006, Astronomy and Astrophysics, 448, 313

Skrutskie, M. F., Cutri, R. M., Stiening, R., et al. 2006, AJ, 131, 1163

Słowikowska, A., Kanbach, G., Kramer, M., & Stefanescu, A. 2009, Monthly Notices of the Royal Astronomical Society, 397, 103

Smith, F. G. 1986, Monthly Notices of the Royal Astronomical Society, 219, 729

Smith, F. G., Jones, D. H. P., Dick, J. S. B., & Pike, C. D. 1988, Monthly Notices of the Royal Astronomical Society, 233, 305

Staelin, D. H. & Reifenstein, E. C. 1968, Science, 162, 1481

Standish, E. M. 1998, Jet Propulsion Laboratory IOM 312.F-98-048

Takata, J. & Chang, H.-K. 2007, The Astrophysical Journal, 670, 677

Thompson, D. J., Bailes, M., Bertsch, D. L., et al. 1999, Astrophysical Journal, 516, 297

Tiengo, A., Mignani, R. P., de Luca, A., et al. 2011, Monthly Notices of the Royal Astronomical Society: Letters, 412, L73

Ulmer, M. P., Park, S., Finley, J. P., Middleditch, J., & Codes, M. J. 1999, Astrophysical Letters and Communications, 38, 29

Williams, B. J., Borkowski, K. J., Reynolds, S. P., et al. 2008, The Astrophysical Journal, 687, 1054

Zampieri, L., Germanà, C., Barbieri, C., et al. 2011, Advances in Space Research, 47, 365

Zhang, L. & Cheng, K. S. 2000, Astronomy and Astrophysics, 363, 575

Zhang, W., Marshall, F. E., Gotthelf, E. V., Middleditch, J., & Wang, Q. D. 2001, The Astrophysical Journal, 554, L177

Zheleznyakov, V. V. & Shaposhnikov, V. E. 1972, Astrophysics and Space Science, 18, 166